Icarus 241 (2014) 373–396

Contents lists available at ScienceDirect

Icarus

journal homepage: www.elsevier.com/locate/icarus

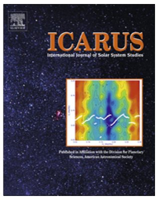

Noncircular features in Saturn's rings II: The C ring

Philip D. Nicholson [a,*], Richard G. French [b], Colleen A. McGhee-French [b], Matthew M. Hedman [c], Essam A. Marouf [d], Joshua E. Colwell [e], Katherine Lonergan [b], Talia Sepersky [b]

[a] *Department of Astronomy, Cornell University, Ithaca, NY 14853, United States*
[b] *Department of Astronomy, Wellesley College, Wellesley, MA 02481, United States*
[c] *Department of Physics, University of Idaho, Moscow, ID 83844, United States*
[d] *Department of Electrical Engineering, San Jose State University, San Jose, CA 95192, United States*
[e] *Department of Physics, University of Central Florida, Orlando, FL 32816, United States*

ARTICLE INFO

Article history:
Received 8 March 2014
Revised 20 June 2014
Accepted 21 June 2014
Available online 10 July 2014

Keywords:
Saturn, rings
Occultations
Planetary rings

ABSTRACT

We present a comprehensive survey of sharp-edged features in Saturn's C ring, using data from radio and stellar occultation experiments carried out by the *Cassini* spacecraft over a period of more than five years. Over 100 occultations are included in the combined data set, enabling us to identify systematic radial perturbations as small as 200 m on the edges of ringlets and gaps. We systematically examine all of the noncircular features in the C ring, refine the eccentricities, precession rates and width variations of the known eccentric ringlets, identify connections between several noncircular gap and ringlet edges and nearby satellite resonances, and report the discovery of a host of free normal modes on ring and gap edges. We confirm a close association between the Titan (or Colombo) ringlet ($a = 77878.7$ km) and the Titan 1:0 apsidal resonance: the apoapse of the ringlet is nearly aligned with Titan's mean longitude, and the pattern speed closely matches Titan's mean motion. Similar forced perturbations associated with the Titan resonance are detectable in more than two dozen other features located throughout the inner C ring as far as 3500 km from the Titan resonance. The inner edge of the Titan ringlet exhibits several strong outer Lindblad resonance (OLR-type) normal modes, and scans of the outer edge reveal inner Lindblad resonance (ILR-type) normal modes. The Maxwell ringlet ($a = 87{,}510$ km), in contrast, appears to be a freely-precessing eccentric ringlet, with post-fit RMS residuals for the inner and outer edges of only 0.23 and 0.16 km, respectively. The best-fitting edge precession rates differ by over 10 times the estimated uncertainty in the rate of the inner edge, consistent with a slow libration about an equilibrium configuration on a decadal timescale. Using self-gravity models for ringlet apse alignment, we estimate the masses and surface densities of the Titan and Maxwell ringlets. The Bond ringlet ($a = 88{,}710$ km), about 17 km wide, shows no free eccentricity but lies near two strong resonances: the Mimas 3:1 inner vertical resonance (IVR) at 88702.2 km and the Prometheus 2:1 ILR at 88713.1 km. We find no measurable perturbation from the Mimas IVR, but a clear $m = 2$ signature of the appropriate phase and pattern speed for the Prometheus ILR on the outer edge of the ringlet, along with free ILR-type normal modes with wave numbers $m = 3, 4, 5, 6$ and 7. The Dawes gap, located at 90,210 km, and its associated embedded ringlet, also show both free and forced perturbations, and as in the case of the Maxwell gap, the outer edge of the Dawes gap appears to be sympathetically forced by the nearby ringlet. The pattern of newly identified normal modes coexisting on the sharp edges of ringlets and gaps is in excellent agreement with theoretical predictions, with ILR-type modes on outer ringlet (and inner gap) edges and OLR-type modes on inner ringlet (and outer gap) edges, representing standing waves between the resonance locations and the ring edges. Modes with larger $|m|$ generally have narrower resonant cavities, and of the dozens of detected normal modes, none has been identified with a resonance radius that falls outside the ring material.

1. Introduction

Saturn's C ring is the innermost and least opaque of the three classical components of the planet's main ring system. It contains

---

* Corresponding author.
E-mail address: nicholso@astro.cornell.edu (P.D. Nicholson).

http://dx.doi.org/10.1016/j.icarus.2014.06.024
0019-1035/

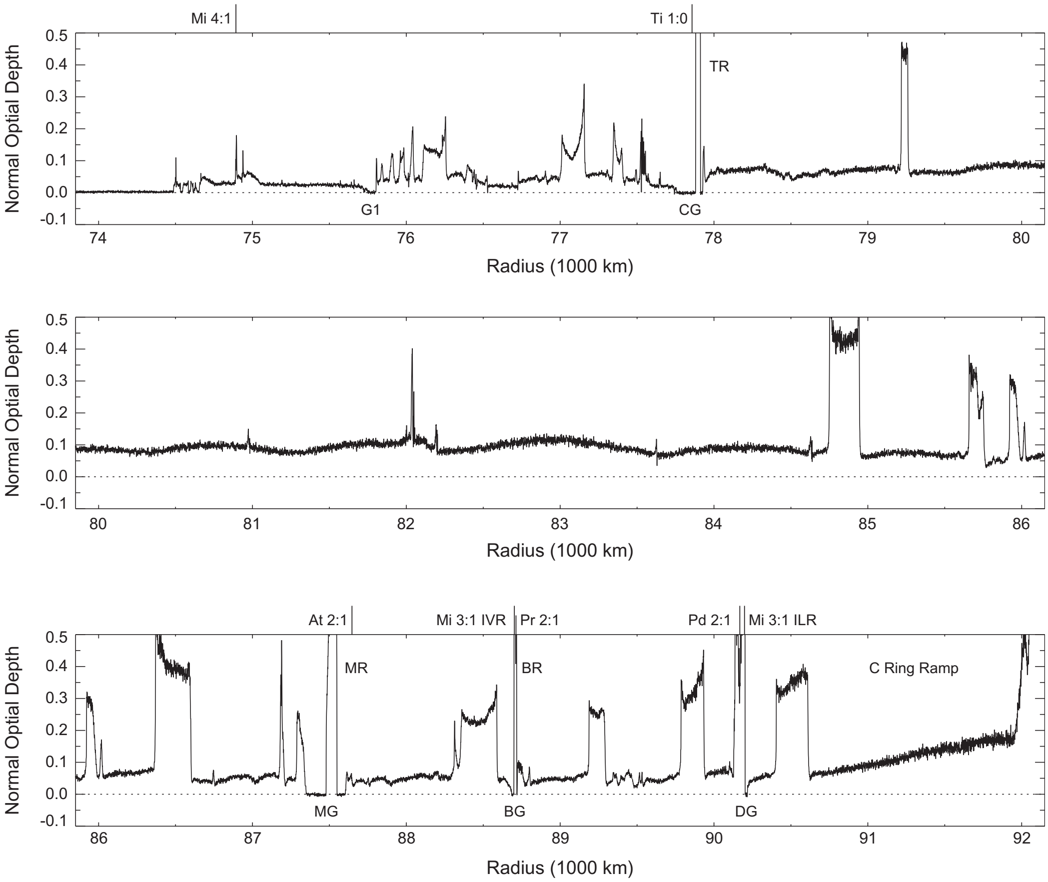

Fig. 1. An optical depth profile of the C ring, derived from the *Cassini* radio occultation on Rev 7. Abbreviations refer to the Titan ringlet (TR) and Colombo gap (CG), the Maxwell gap and ringlet (MG, MR), the Bond gap and ringlet (BG, BR) and Dawes gap (DG). Tick marks across the top of the plot indicate the locations of significant satellite resonances, with Ti = Titan, Mi = Mimas, At = Atlas, Pr = Prometheus and Pd = Pandora.

five significant gaps, four of which contain or are bordered by narrow, optically-thick ringlets (Colwell et al., 2009). Several of the gap edges and all of the associated ringlets are known to be noncircular, as first noted in studies of imaging and occultation data returned by the two *Voyager* spacecraft in 1980 and 1981. In some cases, the observed radial perturbations appear to be driven by resonances with external satellites, while in other instances, notably the Maxwell ringlet, the feature's eccentricity appears to be unforced and likely represents a natural state of dynamical equilibrium. An overall view of the C ring is provided in Fig. 1 (based on Fig. 13.21 in Colwell et al. (2009)) where we have identified the principal gaps and isolated ringlets that are the focus of this study.

Most prominent of the noncircular features are the informally-named Titan ringlet, which inhabits the Colombo gap at 77,880 km, and the Maxwell ringlet located within its eponymous gap at a radius of 87,510 km. Studies of these features by Esposito (1983) and Porco et al. (1984b) demonstrated that they are both well-described by keplerian ellipses, precessing under the influence of Saturn's zonal gravity harmonics. The Titan ringlet, however also happens to be located at a distance where the local apsidal precession rate matches the mean motion of Titan ($22.577^\circ\ \mathrm{d}^{-1}$), and Porco et al. (1984b) concluded that its eccentricity is likely forced by this apsidal resonance.[1] This idea was further pursued by Nicholson and Porco (1988), who used the ringlet's eccentricity to place a constraint on Saturn's zonal gravity harmonics, notably J_6. The Maxwell ringlet, on the other hand, appears to be more akin to the narrow, freely-precessing Uranian rings, and is in fact similar in many of its characteristics to that planet's ϵ ring. Particularly notable are the large gradients in eccentricity across both rings, which are thought to approach the maximum sustainable value (Mosqueira, 1996). In both cases it was proposed that the ring's self-gravity acts to counteract the tendency to differential precession, which would quickly destroy such an eccentric ring if the particles' orbits were subject solely to the planet's gravity (Goldreich and Tremaine, 1979; Porco et al., 1984b). However, subsequent observational and theoretical studies have cast some doubt on this hypothesis, at least in its original form (Marouf et al., 1987; Borderies et al., 1988; Chiang and Goldreich, 2000; Mosqueira and Estrada, 2002).

Much less is known about the C ring's other noncircular features, primarily because their deviations from circularity are about an order of magnitude smaller, and near the limit detectable in *Voyager* data. Porco and Nicholson (1987) and Nicholson et al. (1990) studied the gaps and associated ringlets at $88,720$ km ($= 1.470\ R_S$) and at 90,200 km ($= 1.495\ R_S$) – since renamed the Bond and Dawes gaps, respectively. Each is associated with one of the strongest satellite resonances in the C ring: the inner edge of the Bond ringlet coincides with the Mimas 3:1 inner vertical resonance (IVR), while the inner edge of the Dawes gap (or the outer edge of the 1.495 R_S ringlet) coincides with the Mimas 3:1 inner Lindblad resonance (ILR). The situation is further complicated, however, by the presence of two other, only slightly weaker, resonances: the 2:1 ILRs due to the F ring shepherd satellites, Prometheus and Pandora. Porco and Nicholson (1987) found significant departures from circularity for both the Bond ringlet and the inner edge of the Dawes gap, the latter at the several km level, but were unable to demonstrate a clear connection with any of the four possible satellite resonances.

---

[1] This is in fact a special case of an inner Lindblad resonance (see Appendix A), and it is also referred to as the 1:0 ILR.

With the arrival of the *Cassini* spacecraft at Saturn in July 2004, a new era in studies of Saturn's rings has opened and it is now possible to re-examine the nature and dynamical origins of these features. In particular, radio occultations observed using the spacecraft's three-frequency communications signal and stellar occultations observed by the ultraviolet and near-infrared spectrometer instruments have provided several hundred radial profiles of the rings, at radial resolutions in the 10–400 m range. Spanning a period of almost six years, or at least 90 precessional cycles of orbits in the C ring, this dataset is vastly improved over that provided by the *Voyager* flybys and permits us to pose much more detailed questions about the structure and dynamics of the noncircular features.

In the first paper in this series, we examined the shape and dynamics of the outer edge of the B ring (Nicholson et al., 2014), long known to be controlled and perturbed by the Mimas 2:1 ILR. Confirming a result first obtained by Spitale and Porco (2010) from an analysis of *Cassini* images, we found that this sharp edge is perturbed not only by the Mimas resonance, with the expected azimuthal variations with wavenumber $m = 2$, but also by radial distortions with $m = 1$, 3, 4 and 5. These non-resonant perturbations are thought to arise from normal modes in the ring, which involve density waves reflected by the very sharp outer edge of the ring and trapped in what amounts to a resonant cavity in the outermost part of the B ring (Spitale and Porco, 2010).

In the present paper, we systematically examine all of the noncircular features in the C ring, with a view to refining the eccentricities, precession rates and width variations of the known eccentric ringlets and establishing direct connections, if any, between several noncircular gap and ringlet edges and nearby satellite resonances. In the course of this work, we have uncovered several more examples of spontaneously generated normal modes on the edges of both ringlets and their host gaps. We have also searched for additional, previously unsuspected noncircular features in the C ring.

In a subsequent paper (French et al., 2014a), hereafter Paper III, we will address noncircular features in the Cassini Division.

An essential prerequisite to these studies is the establishment of an accurate absolute radius scale for Saturn's rings, via the identification of a set of circular fiducial features to which suspected variable features can be referred. This task must, by its very nature, include data from as many observations as possible, and from features across the entire ring system. To some extent, this is an iterative process, with several putative fiducial features having been discovered to be noncircular during the course of the study. It is also of lesser interest to those readers who wish only to know about the noncircular features. We thus defer this discussion to a separate paper (French et al., 2014b), referred to as Paper IV, and provide only an overview of the main results here, in Section 3.

As one of the principal (and unexpected) results of this investigation is the identification of numerous normal modes on the edges of narrow ringlets and gaps in the C ring and Cassini Division, we begin with a review of this concept in Section 2. In Section 3 we provide a brief recap of the occultation dataset, while we discuss our orbit-fitting procedure and the underlying dynamical models in Section 4. In Sections 5–8 we present our results for the Titan and Maxwell ringlets (and their associated gaps) and for the Bond and Dawes gaps, in turn. In Section 10 we present updated width–radius relations and self-gravity models for the Titan and Maxwell ringlets, while a review of the normal modes identified in this work is presented in Section 11. Section 12 summarizes our findings concerning resonantly-forced perturbations, and in Section 13 we provide constraints on Saturn's gravity field provided by the Titan and Maxwell ringlets. We summarize our conclusions in Section 14. A brief review of the relevant resonance dynamics and essential formulae is provided in Appendix A.

2. Normal modes

The concept of normal modes in planetary rings was introduced by Borderies et al. (1986), based on their model for viscous interactions in dense, self-gravitating rings, and discussed in more detail in the context of narrow rings by Longaretti and Rappaport (1995). This model predicts that outward- and inward-propagating density waves could arise spontaneously in such a ring and, in the presence of a feedback mechanism, could lead to finite-amplitude standing waves in the ring. The presence of a sharp outer edge can provide this feedback, as an outward-propagating trailing density wave will be reflected as an inward-propagating leading wave with the same number of arms m and pattern speed Ω_p (see below). In a narrow ringlet, the reverse process can then happen at the inner edge, converting the leading wave back into a trailing wave. Interference between the two traveling waves then gives rise to a standing wave, which is trapped between the inner and outer edges of the ringlet. Fundamental to this picture of normal modes as standing density waves is the basic fact that, for any particular value of m, leading and trailing waves rotate with the same angular speed but propagate in opposite radial directions (Shu, 1984).

Such modes are unrelated to any external agency, but their geometry and frequencies are closely akin to the perturbations produced by inner or outer Lindblad resonances due to distant satellites. In particular, the radial displacements associated with such modes vary with longitude λ and time t as $e^{i(m\lambda-\omega t)}$, where the frequency ω is given by

$$\omega \equiv m\Omega_p = (m-1)n + \dot{\varpi}_{\rm sec}. \tag{1}$$

Here, n is the local keplerian mean motion and $\dot{\varpi}_{\rm sec}$ is the apsidal precession rate due to Saturn's gravity field, as given by Eq. (3) below. Ω_p, known as the *pattern speed*, is the angular rotation rate of the perturbation in inertial space. In this expression, a positive value of m corresponds to an ILR-type normal mode, while a negative value of m corresponds to an OLR-type normal mode, as defined below. Note that, in either case, Ω_p is positive.

A requirement for such an amplification process to work, in the presence of viscous (*i.e.,* collisional) damping, is that the wavelength of the density waves be comparable to the width of the ringlet. This in turn favors $m = 1$ normal modes, as their wavelengths are much longer than those of their siblings (Shu, 1984). Indeed, it is possible to reinterpret a typical precessing eccentric ringlet as an example of such an $m = 1$ normal mode, as the predicted pattern speed is simply $\Omega_p = \dot{\varpi}_{\rm sec}$ (Longaretti, 1989).

Direct observational evidence for normal modes in narrow ringlets (other than the familiar $m = 1$ modes) was first provided by the Uranian γ and δ rings, where French (1988a) showed that the observed nonkeplerian distortions could be interpreted as normal modes with $m = 0$ and $m = 2$, respectively. With widths of $\sim$5 km, these two rings are sufficiently narrow for the above double-reflection process to work.

Perhaps not so immediately apparent is the fact that similar normal modes can exist at the sharp inner or outer edge of a broad ring. In a differentially-rotating disk, density waves with a given value of $|m|$ and a particular pattern speed can propagate only in a limited radial range. The limits of this range are defined by the corresponding *inner and outer Lindblad resonances*, as defined by Eq. (1) for positive and negative values of m. Long trailing waves propagate away from either an inner or outer Lindblad resonance, towards the *corotation resonance* where $\Omega_p = n$, while long leading waves propagate towards either Lindblad resonance.[2] Leading

---

[2] In a gaseous disk, both short and long-wavelength waves are possible, but the former are essentially sound waves and have no relevance to particulate rings.

waves are reflected when they encounter either resonance, being converted to long trailing waves (Shu, 1984).

Consider first a ring with a sharply-defined *outer* edge, within which the viscous overstability mechanism of Borderies et al. (1986) spontaneously generates a wide spectrum of leading and trailing density waves, which then propagate inwards and outwards from their source regions. Inward-propagating waves will viscously damp and disappear. But an outward-propagating trailing wave will encounter the gap edge and reflect back towards its source as a leading wave with the same m-number and pattern speed. If the pattern speed of these waves is such that the inner Lindblad resonance (ILR) – *i.e.,* the radius where Eq. (1) is exactly satisfied for a positive value of m – is within a few radial wavelengths interior to the ring edge, then the leading wave will reflect at this virtual resonance and reappear as an outward-propagating trailing wave, thus providing the desired feedback mechanism. The result is a standing wave that is trapped between the ILR and the outer ring edge, with a pattern speed appropriate to a resonance location slightly *interior* to the ring edge. We refer to the resulting distortion as an ILR-type normal mode, for short.

Spitale and Porco (2010) and Nicholson et al. (2014) identified normal modes of exactly this type with $m = 1$, 3, 4 and 5 at the outer edge of Saturn's B ring. Each of these modes was found to have a pattern speed which corresponds to an ILR located a few tens of km interior to the ring edge, except for the $m = 1$ mode whose radial wavelength is longer, and for which the resonant cavity is substantially wider.

The basic wave-generation process is identical at the *inner* edge of a broad ring, but in this case a spontaneously-generated inward-propagating trailing wave reflects at the ring's inner edge, becoming an outward-propagating leading wave. Such a wave can then reflect at its *outer* Lindblad resonance (OLR) – *i.e.,* the radius where Eq. (1) is exactly satisfied for a negative value of m – again providing feedback and establishing a resonant cavity. As before, the pattern speed is given by Eq. (1), but with a negative m, and we refer to the resulting distortion as an OLR-type normal mode. In this case, the pattern speed is expected to be that appropriate to a resonance location slightly *exterior* to the ring edge.

Unlike the situation in narrow ringlets, such as the Uranian γ and δ rings, the normal modes on the inner and outer edges of a broad ring are confined to narrow resonant cavities near each edge and do not communicate with one another. They are thus quite independent. It is also possible, at least in the small-amplitude regime where the waves are linear, to have multiple normal modes co-existing at a single ring edge. The dispersion relation for density waves implies that the width of each resonant cavity scales as $\Sigma/|m-1|$, where Σ is the background surface mass density (Nicholson et al., 2014).

It is important to recognize the distinction between resonantly-forced perturbations and normal modes, both of which satisfy Eq. (1). In the former case, the m-value and pattern speed are determined by the perturbing satellite and our equation serves implicitly to determine the resonant radius $a_{\rm res}$ where the perturbations are expected to be strongest. In the latter case, the same equation specifies the *allowed* angular frequencies of the normal modes that can exist at (or near) any given radius for different values of m. But since both forms of perturbation obey the same underlying dynamics and thus Eq. (1), it follows that an $m-$lobed distortion at a particular ring edge will have almost the same pattern speed regardless of whether it is externally-forced or arises as a normal mode. This can sometimes lead to ambiguities of interpretation.

Normal modes with $m = 0$ are a special case, inasmuch as their radial and density perturbations are axisymmetric and their pattern speed is zero. However, their temporal oscillation frequency, $\omega = |m\Omega_p|$ is nonzero and is equal to $n - \dot{\varpi}_{\rm sec} = \kappa$, the local epicyclic frequency. Neither leading nor trailing, $m = 0$ waves can propagate both inwards and outwards, but it can be shown that in this case only the outer Lindblad resonance exists (Shu, 1984). Normal modes with $m = 0$ are thus expected to exist only at inner ring edges, or outer gap edges.

3. Observations

Our data set for this paper includes *Cassini* ring occultation observations from the VIMS (Brown, 2004), UVIS (Colwell et al., 2010), and RSS (Kliore, 2004) instruments obtained between May 2005 and October 2010. It is a subset of the observations used in Paper III for our analysis of Cassini Division features and to establish the absolute radius scale for the rings in Paper IV, which papers will contain a full description of the data analysis and circumstances of each occultation. For our present purposes, we refer the reader to French et al. (2010a) and Nicholson et al. (2014) for a summary of the key characteristics of the *Cassini* radio and stellar occultation experiments, as well as a description of our techniques for measuring the locations of individual ring features and correcting for spacecraft trajectory errors in the reconstruction of the occultation geometry.

For sharp-edged ring features, individual measurements of the edge location have typical uncertainties of 100–200 m, and in some of the best cases, the RMS residuals for orbit fits to nominally circular features are as low as 100 m. At present, we estimate the accuracy of the radius scale from occultation to occultation to be about 200 m (based on these fits and on a comparison of predicted and observed relative phases of individual density wave crests in the C ring by Hedman and Nicholson (2013)). The *absolute* accuracy of the radius scale is estimated to be about 300 m, limited primarily by current uncertainties in the direction and precession rate of Saturn's pole (Jacobson et al., 2011). These uncertainties are likely to be reduced when more recent *Cassini* observations are incorporated into the global solution for Saturn's ring geometry.

4. Ring orbit determination

4.1. Dynamical models

Our least-squares fitting program uses a standardized kinematic model for all ring edges, with a set of free parameters that can be selectively included or excluded, as desired for specific features. The basic model is of a precessing, inclined keplerian ellipse, specified by the usual expression:

$$r(\lambda, t) = \frac{a(1-e^2)}{1+e\ \cos f}, \tag{2}$$

where the true anomaly $f = \lambda - \varpi = \lambda - \varpi_0 - \dot{\varpi}(t - t_0)$. Here, r, λ and t are the radius, inertial longitude and time of the observation, a and e are the ring edge's semi-major axis and eccentricity, ϖ and $\dot{\varpi}$ are its longitude of periapse and apsidal precession rate, and t_0 is the epoch of the fit. For most features, we assume that the ring edge lies in Saturn's mean equatorial plane, assuming a constant rate and direction for the precession of Saturn's pole over the course of the *Cassini* observations considered here. For inclined features, we include three additional parameters: i (inclination relative to the mean ring plane), Ω_0 (longitude of the ascending node) and $\dot{\Omega}$ (nodal regression rate), and compute the intercept point of the ray from the spacecraft to the Earth or star with the specified inclined ring plane. The zero-point for the inertial longitudes λ, ϖ_0 and Ω_0 (as well as δ_m and ϵ_m below) is the ascending node of Saturn's equator on the Earth's equator of J2000. All of our models use a common epoch of 2008 January 1, 12:00 UTC = JD 245 4467.0, as in Paper I. As *a priori* values for $\dot{\varpi}$ and $\dot{\Omega}$ we calculate the expected precession rates $\dot{\varpi}_{\rm sec}$ and $\dot{\Omega}_{\rm sec}$ from the combined effects of Saturn's zonal gravity harmonics J_2, J_4, and J_6 (Nicholson and Porco, 1988;

French et al., 1982) and the secular precession induced by the planet's major satellites (Null et al., 1981):

$$\dot{\varpi}_{\rm sec} = \sqrt{\frac{GM}{a^3}}\left\{\frac{3}{2}J_2\left(\frac{R}{a}\right)^2(1+e^2-2\sin^2 i) - \frac{15}{4}J_4\left(\frac{R}{a}\right)^4 + \left[\frac{27}{64}J_2^3 - \frac{45}{32}J_2J_4 + \frac{105}{16}J_6\right]\left(\frac{R}{a}\right)^6 + \frac{1}{4}\sum_j\frac{m_j}{M}\alpha_j^2 b_{3/2}^1\right\} \qquad (3)$$

$$\dot{\Omega}_{\rm sec} = -\sqrt{\frac{GM}{a^3}}\left\{\frac{3}{2}J_2\left(\frac{R}{a}\right)^2\left(1+e^2-\frac{1}{2}\sin^2 i\right) - \left[\frac{9}{4}J_2^2 + \frac{15}{4}J_4\right]\left(\frac{R}{a}\right)^4 + \left[\frac{351}{64}J_2^3 + \frac{315}{32}J_2J_4 + \frac{105}{16}J_6\right]\left(\frac{R}{a}\right)^6 + \frac{1}{4}\sum_j\frac{m_j}{M}\alpha_j^2 b_{3/2}^1\right\}, \qquad (4)$$

where the summation is carried out over 7 external satellites of mass m_j and orbital radius a_j, $\alpha_j = a/a_j$, and $b_{3/2}^1(\alpha_j)$ is a Laplace coefficient as defined by Brouwer and Clemence (1961).[3] M and R are the mass and equatorial reference radius of Saturn, respectively.

In addition to the keplerian orbit, our model for any given ring allows for other modes of radial distortion, each of which is specified by an equation of the form:

$$\Delta r(\lambda, t) = -A_m\ \cos(m\theta), \qquad (5)$$

where

$$\theta = \lambda - \Omega_p(t - t_0) - \delta_m \qquad (6)$$

and m is the number of radial minima and maxima in the pattern. This expression describes free or normal modes of oscillation, as described in Section 2, where A_m and δ_m are the mode's radial amplitude and phase,[4] respectively, and the pattern speed Ω_p is its angular rotation rate in inertial space. As discussed above, Ω_p is expected to be close to that of a Lindblad resonance located at the particles' orbit (Borderies and Longaretti, 1987; French et al., 1991), as given by Eq. (1). Thus we take as an *a priori* estimate

$$\Omega_p \simeq [(m-1)n + \dot{\varpi}_{\rm sec}]/m, \qquad (7)$$

where the mean motion n and apsidal precession rate $\dot{\varpi}_{\rm sec}$ – given by Eq. (3) – are evaluated at the semimajor axis of the edge. As noted in Section 2, a positive value of m corresponds to an ILR-type normal mode, while a negative value of m corresponds to an OLR-type normal mode. We expect to find the former at the outer edges of ringlets or the inner edges of gaps, and the latter at the inner edges of ringlets or the outer edges of gaps. In either case, Ω_p is positive. For orbits about an oblate planet, n is given by the expression (R.A. Jacobson, private communication, 2009), based on the epicylic expression derived by Borderies-Rappaport and Longaretti (1994):

$$n = \sqrt{\frac{GM}{a^3}}\left\{1 + \frac{3}{4}J_2\left(\frac{R}{a}\right)^2(1+4e^2-16\sin^2 i) - \left[\frac{15}{16}J_4 + \frac{9}{32}J_2^2\right]\left(\frac{R}{a}\right)^4 + \left[\frac{27}{128}J_2^3 + \frac{45}{64}J_2J_4 + \frac{35}{32}J_6\right]\left(\frac{R}{a}\right)^6 - \sum_j\frac{m_j}{M}\left[\alpha_j^2 b_{3/2}^1 - \alpha_j^3 b_{3/2}^0\right]\right\}, \qquad (8)$$

where again the external satellite terms are very small and may be neglected for our purposes.

For each mode, the additional fit parameters are A_m, Ω_p and δ_m. We note that an $m = 1$ ILR-type mode is equivalent, at least to first order in e, to a precessing keplerian ellipse with $A_1 = ae$, $\Omega_p = \dot{\varpi}_{\rm sec}$ and $\delta_1 = \varpi_0$, the longitude of pericenter at $t = 0$.

Eq. (5) can also be used to describe radial perturbations forced by a Lindblad resonance with an external satellite, the principal difference being that in this case the pattern speed, m-value, and phase are all determined by the satellite's orbital parameters, and Eq. (1) now serves to specify implicitly the exact resonance location $a_{\rm res}$. The reader is referred to Appendix A for explicit expressions for Ω_p and δ_m for each of the four Lindblad resonances suspected to be relevant for the C ring features we study here.

Our model also includes terms describing possible vertical oscillations, using an equation of the form:

$$z(\lambda, t) = B_m\ \sin(m\theta), \qquad (9)$$

with

$$\theta = \lambda - \Omega_p(t - t_0) - \epsilon_m. \qquad (10)$$

Again, this expression can accommodate either free or resonantly-forced modes, as appropriate. B_m and ϵ_m are the mode's vertical amplitude and phase, respectively, and in this case the pattern speed Ω_p is expected to be close to that of a vertical resonance located at the particles' orbit. We therefore take as an *a priori* estimate

$$\Omega_p \simeq [(m-1)n + \dot{\Omega}_{\rm sec}]/m, \qquad (11)$$

where $\dot{\Omega}_{\rm sec}$ is the nodal regression rate as given by Eq. (4). In this expression, a positive value of m corresponds to an IVR-type normal mode, or to a forced perturbation at a satellite IVR. Note that an $m = 1$ mode is equivalent, to first order in i, to an inclined keplerian orbit with $B_m = a\ \sin i$, $\Omega_p = \dot{\Omega}_{\rm sec}$ (the nodal regression rate) and $\epsilon_1 = \Omega_0$ (the longitude of the ascending node at $t = 0$). See Appendix A for explicit expressions for Ω_p and ϵ_m for the Mimas 3:1 IVR, the most important vertical resonance in the C ring.

Our nominal model for a given ringlet or gap edge thus has up to $7 + 3n$ free parameters: 4 or 7 for the precessing keplerian ellipse and three for each of the n additional forced and/or normal modes.

4.2. Ring feature fits

The *Cassini* occultations used for this study comprise nearly 150 separate one-dimensional scans across Saturn's rings, obtained under a wide range of viewing geometries, ring opening angles, and spacecraft distances from the rings. We determine the orbital characteristics of individual ring and gap edges by first measuring the observed times of these features in each occultation profile, and then using a well-tested least-squares orbit-fitting code to solve for the ring orbital elements that give the best match to the ensemble of observations. The observed times, defined as the equivalent half-light times at normal incidence, are determined by least squares fits of a standard template to the shape of each feature, as described in detail in French et al. (2010a). The ring event times from such fits are converted into a set of two-dimensional intercept points in the ring plane penetrated by the occultation, based on the assumed inclination for the ring, the orientation of Saturn's pole in inertial space, and the heliocentric time-dependent positions of the radiation source and the observer. The occultation geometry is computed using the heliocentric vector algorithm described in Appendix A of French (1993), with minor modifications as noted in French et al. (2010a). The algorithm incorporates non-relativistic light travel time corrections (and general relativistic bending of starlight by Saturn for Earth-based stellar occultation observations, but not included as part of the present study). For the *Cassini* stellar occultations considered here, we use the Hipparcos catalog star positions (ESA, 1997), account-

---

[3] Note that in these expressions, a is the mean, or geometric, semimajor axis of the ring feature as defined in Eq. (2), rather than the osculating semimajor axis, which differs by an amount of $O(aJ_2(R/a)^2)$ or several hundred km in the outer C ring. The external satellite contributions to the precession rates are small: of order $1.4 \times 10^{-4}\,^\circ\,{\rm d}^{-1}$ at the orbit of the Titan ringlet (Nicholson and Porco, 1988) and increasing to $5 \times 10^{-4}\,^\circ\,{\rm d}^{-1}$ in the outer A ring. Solar and general-relativistic perturbations are even smaller and may be neglected for our purposes.

[4] More specifically, δ_m is the longitude at epoch of one of the m radial minima.

ing for parallax and proper motion computed instantaneously for each individual ring measurement. We use the most recent reconstructed *Cassini* spacecraft trajectory files, planetary ephemerides, and planetary constants files and the SPICE software toolkit from NASA's Navigation and Ancillary Information Facility (Acton, 1996).[5]

A key requirement for both accurate orbit determinations and precise identification of resonance locations is a reliable absolute radius scale for the rings. Previous solutions for the geometry of Saturn's ring system made use of *Voyager* radio and stellar occultations (Nicholson et al., 1990), augmented by extensive Earth-based observations of the occultation of 28 Sgr in 1989 (French, 1993) and subsequent Hubble Space Telescope stellar occultations (Bosh, 1994). For this work, we have derived an absolute ring radius scale based on *Cassini* occultation data alone, both to take advantage of the sheer abundance and high quality of these observations, and to reduce the systematic errors in the solution resulting from uncertainties in the direction of Saturn's rotational axis due to precession. As part of this solution, we also make first-order corrections to the spacecraft trajectory at the time of each stellar or radio occultation chord, since the *a priori* positional uncertainty in the *Cassini* spacecraft location is ~1 km and (especially for grazing viewing geometries) small errors in spacecraft position can be amplified several-fold in the derived ring plane radius.

We proceed in an iterative fashion by identifying a set of putative circular and equatorial ring features, and then fitting simultaneously for their keplerian orbital elements and for an along-track timing offset for each relevant segment of the spacecraft trajectory as a simple, one-parameter correction for trajectory errors and/or slight errors in the catalog positions of the occulted stars. After each round of fits, we eliminate candidate rings that are measurably non-circular or inclined or show large RMS errors (due, perhaps, to uncertainties in measuring the edge location, or to intrinsic unmodelled variations in the shape of the ring), and retain only those occultation events with four or more circular features. In the end, we identified ~60 circular features in the C and B rings, and in the Cassini Division (each with from 83 to 142 individual measurements, for a total of over 6000 data points) to determine trajectory offsets and an absolute radius scale to use for the remainder of this study. No circular features were identified in the A ring.

RMS residuals for these circular features are in all cases less than $\sigma = 0.25$ km, and in some cases below 0.10 km. These residuals should not be confused with the *relative* accuracies of the orbital radii of different circular features, or the absolute accuracy of the radius scale itself. For a feature with $N = 100$ individual measurements, the corresponding statistical error in the fitted semimajor axis is $\sim\sigma/\sqrt{N}$, or a few tens of meters, as seen below in the tabulated fit results for individual ring features. This represents the jitter in the fitted radial position resulting from the statistical scatter in the residuals arising from measurement errors in the locations of the ring edges themselves, unmodelled ring dynamical effects, and/or residual systematic errors in the geometric solution such as stellar position errors. A separate question altogether is the *absolute* accuracy of the radius scale, which depends primarily on uncertainties in the precession and nutation of Saturn's rotational pole due primarily to solar torques transmitted to the planet itself via Titan and Iapetus. The polar precession rate is of interest in its own right because it depends strongly on the planet's moment of inertia, an important constraint on models of Saturn's interior, but an accurate determination of the pole's precession rate from occultations will require inclusion of results from pre-*Cassini* occultations, which is beyond the scope of this work. For present purposes, we estimate the accuracy of the radius scale from occultation to occultation to be about 200 m, based on comparisons of fit results, and its *absolute* accuracy to be about 300 m. As a point of comparison, our current radius scale agrees to within ~1 km with that derived by French (1993). Additional details of this procedure will be described in Paper IV.

Although in-plane perturbations manifest themselves directly as radial offsets with respect to a keplerian model, out-of-plane perturbations must be handled differently. In such cases, the apparent radial offset of the ring depends on the vertical displacement z, on the elevation of the stellar line of sight with respect to the ring plane B_*, and on the longitude of observation λ. Denoting the inertial longitude of the line of sight to the star as λ_*, then some straightforward geometry shows that the *apparent radial displacement* of the ring segment in the occultation profile is given by (Nicholson et al., 1990; Jerousek et al., 2011):

$$\Delta r = -\frac{z\cos\phi}{\tan B_*}, \tag{12}$$

where $\phi = \lambda - \lambda_*$. For vertically-perturbed rings, we add the above term to our ring model, where $z(\lambda, t)$ is given by Eq. (9).

For any particular star, both B_* and λ_* are fixed, but we see that Δr depends on z and ϕ. For occultations near the ring ansae (where $\phi \simeq 90^\circ$ or 270°), the radial displacement is almost zero, even if z is substantial. But for occultation cuts near the sub-spacecraft point or its antipode, where $\phi \simeq 180^\circ$ or 0°, $|\Delta r| \simeq z/\tan B_*$. In such a favorable situation, and if B_* is small, the apparent radial displacement can be much greater than z. In searching for the signatures of vertical perturbations, or in placing an upper limit on them, we have found it useful to plot Δr vs $|\cos\phi/\tan B_*|$ and look for a correlation between these two quantities.

We evaluate the goodness of fit for a particular model relative to its competitors using the reduced χ^2 statistic, defined by

$$\chi^2 = \frac{1}{N - N_p}\sum [r_{\rm obs}(\lambda, t) - r_{\rm mod}(\lambda, t)]^2, \tag{13}$$

where N is the number of independent data points and $N' = N - N_p$ is the number of degrees of freedom for the particular fit. This is expressed more intuitively in terms of the root-mean-square residual per degree of freedom, $\sigma = \sqrt{\chi^2}$.

Note that we do not weight the individual data points, primarily because we suspect that the dominant errors are systematic rather than statistical in nature. These can include errors in the geometric reconstruction for a particular occultation, due for example to an unmodelled spacecraft trajectory error, or to a ringlet edge being indistinct or otherwise badly-behaved and thus difficult to measure accurately. Since the RMS residuals of an orbit fit vary substantially from ring to ring, we fit each ring separately and scale the nominal errors in the fitted orbital parameters by σ. This is an appropriate procedure when post-fit residuals are well represented by a gaussian distribution, which we find to be the case for all of the fits reported here.

As in Paper I, in many cases we have found it useful to search for possible free or forced modes, and distinguish these from apparent perturbations with little statistical significance. This is done by first fitting and removing a standard keplerian model, plus any already-identified normal modes, and saving the residuals. We then employ a spectral-scanning program which systematically scans through a specified range of pattern speeds for a given value of m, centered on the expected value. At each value of Ω_p, this program fits a 2-parameter model specified by Eq. (5) or (9) to the residuals. An unusually large amplitude occurring at or very close to the expected value of Ω_p, combined with a sharp drop in the post-fit residuals, indicates the likely presence of a real mode. Such mode-scanning can be done for either purely radial or vertical

---

[5] Available online at ftp://naif.jpl.nasa.gov/pub/naif/.

perturbations, and can even be used to search for an ordinary inclination (*i.e.,* Eq. (9) with $m = 1$) when the nodal regression rate is uncertain.

Our standard procedure is first to fit a standard precessing keplerian ellipse to the data, remove this signature from the measured radii, and then carry out a sequential search for any non-zero inclination and normal modes using our spectral scanning program. If a mode with a significant amplitude is identified, its amplitude, pattern speed and phase are included as additional fit parameters and the fit is redone. Residuals from this new fit are then scanned for additional, weaker modes. This procedure is iterated until no new statistically significant modes are found in the spectral scans. In general we search for all modes with values of m from −15 to +15, after first checking for any predicted resonantly-forced perturbations. In most cases, the agreement is excellent between the pattern speeds derived by spectral scanning and from the least-squares fits, but the amplitudes vary somewhat when all parameters are permitted to float together. Our tabulated parameters are always from the final least-squares fit.

5. Titan ringlet

The so-called Titan (or Colombo) ringlet is a prominent narrow ringlet that occupies the outer third of the 170 km-wide Colombo gap in the inner C ring, at a mean radius of ~77,880 km. It is on average ~23 km wide and generally appears completely opaque in occultation profiles. Both edges are invariably sharp at the 100 m level (Jerousek et al., 2011) and are readily measured. A series of stellar occultation profiles of the gap and its ringlet are shown in Fig. 2, arranged to illustrate its relationship with the orbital longitude of Titan. As originally discussed by Porco et al. (1984b), the *apoapse* of the ringlet is roughly aligned with the mean longitude of Titan, which is the anticipated orientation for a set of forced ring particle orbits located exterior to the Titan apsidal resonance (see Appendix A).

Keplerian model fits to both edges of the Titan ringlet are shown in Fig. 3 and summarized in Table 1. Listed here for each edge are the best-fitting semimajor axis a, radial amplitude ae, longitude of pericenter ϖ_0, and the apsidal precession rate $\dot{\varpi}$, as well as the number of data fitted N and post-fit RMS residual σ. We find radial amplitudes of 17.4 and 27.2 km for the inner and outer edges, respectively, and apsidal precession rates and periapse longitudes for both edges that are equal to within their uncertainties. The final two columns, labeled $\Delta\dot{\varpi}$ and $\Delta a_{\dot{\varpi}}$ in Table 1, specify the difference between the fitted precession rate and the calculated value (from Eq. (3)) at the fitted semimajor axis, and the corresponding amount by which the fitted semimajor axis would have to be shifted to match the observed value of $\dot{\varpi}$. The latter is given by $\Delta a_{\dot{\varpi}} = \Delta\dot{\varpi}/(d\dot{\varpi}/da)$.

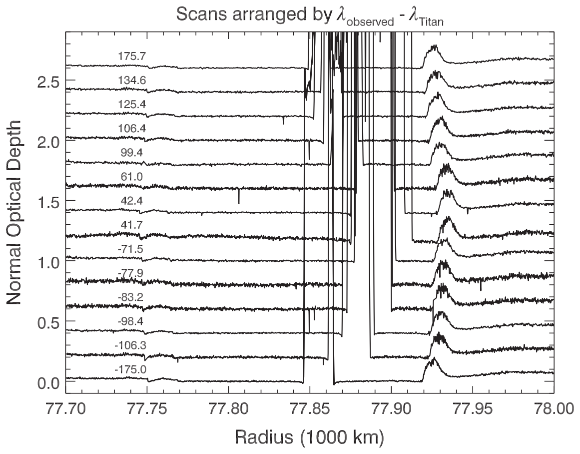

Fig. 2. The region of the Colombo gap and Titan ringlet as seen in a series of 14 optical depth profiles derived from VIMS γ Cru occultations with very similar geometry. The individual profiles are offset vertically and arranged in order of increasing longitude relative to Titan ($\lambda - \lambda_T$, as labeled in each profile) to illustrate the relation of the $m = 1$ radial perturbation to the position of the satellite. The Titan 1:0 resonance is located at a radius of 77857.4 km (see text). Note that, in addition to the ringlet, both gap edges have visible eccentricities (see text).

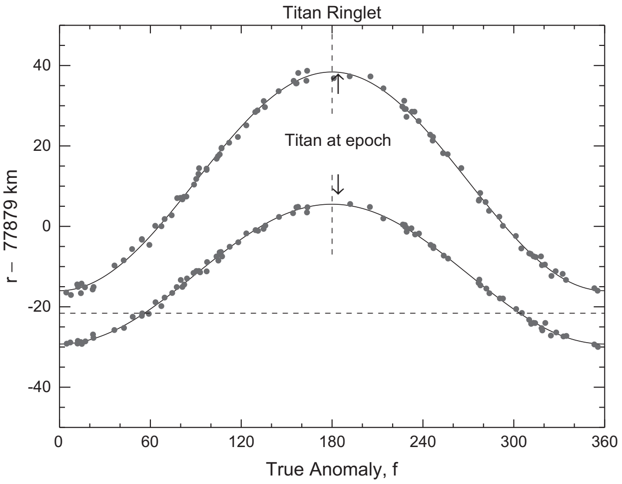

Fig. 3. Measurements of the radii of the inner and outer edges of the Titan ringlet, as a function of true anomaly, $f = \lambda - \varpi$. Solid lines show the best-fitting keplerian models derived separately for both edges. Arrows indicate the mean longitude of Titan at the epoch of the fit, while the horizontal line shows the predicted radius of the apsidal (or 1:0) resonance at 77857.4 km, where $\dot{\varpi}_{\text{sec}} = n$ (Titan).

The mean semimajor axis of the ringlet (computed as the average of the inner and outer edge values) is $\bar{a} = 77878.7$ km, 21.3 km outside the theoretical location of the Titan apsidal resonance $a_{\text{res}} = 77857.4$ km, as calculated using the latest published estimates for Saturn's zonal gravity harmonics (see Appendix A). Furthermore, the best-fitting apsidal rates of $22.5750 \pm 0.0008^\circ\ \text{d}^{-1}$ and $22.5756 \pm 0.0008^\circ\ \text{d}^{-1}$ for the inner and outer edges are much closer to Titan's mean motion of $22.5770^\circ\ \text{d}^{-1}$ than they are to the local precession rates given by Eq. (3). This can be seen from the values of $\Delta a_{\dot{\varpi}}$ in Table 1, which show that the fitted values of $\dot{\varpi}$ for both edges correspond to a common radius of ~77,856 km. This is ~23 km interior to the ringlet's mean radius, but within 1 km of a_{res}.

The close association between this ringlet and the Titan 1:0 resonance is further strengthened by the observation that the pericenter longitudes of both edges differ from the mean longitude of Titan at epoch by 176°, very close to the expected value of 180° for orbits exterior to a_{res}. Further discussion is deferred to Section 12.1 where we also examine other nearby resonantly-forced features in the C ring.

While the keplerian fits to both edges of the Titan ringlet are quite good, their residual scatter is significant, as is evident from Fig. 3. The RMS residuals for pure keplerian fits are 3.0 km and 2.1 km for the inner and outer edges, respectively. These are considerably larger than the measurement errors for such well-defined edges and strongly suggest the presence of additional perturbations. Scans for normal modes reveal the presence of a strong $m = 0$ mode on the inner edge, with an amplitude of 3.7 km, as illustrated in Fig. 4. In addition, we find evidence for weaker OLR-type modes on this edge with $m = -2$ and -5 and amplitudes of 0.8 and 0.5 km. Similar scans of the outer edge reveal three potential ILR-type modes with $m = 2$, 3 and 4 and amplitudes that vary from 0.9 to 1.6 km.

Our full suite of normal modes for both edges is documented in Table 1, where we list for each mode the m-value, the best-fitting

Table 1
Titan ringlet and Colombo gap orbital elements.

ID	Feature	N	a (km) rms (km)	m	ae (km) $a\sin i$ (km) A_m (km)	$\varpi_0(^\circ)$[a] $\Omega_0(^\circ)$ $\delta_m(^\circ)$	$\dot\varpi(^\circ/\mathrm{d})$ $\dot\Omega(^\circ/\mathrm{d})$ $\Omega_p(^\circ/\mathrm{d})$	$\Delta\dot\varpi(^\circ/\mathrm{d})$ $\Delta\dot\Omega(^\circ/\mathrm{d})$ $\Delta\Omega_p(^\circ/\mathrm{d})$	$\Delta a_{\dot\varpi}$ (km) $\Delta a_{\dot\Omega}$ (km) Δa_p (km)
487	Colombo gap IEG		77747.89 ± 0.04	1	3.11 ± 0.06	96.90 ± 0.88	22.57346 ± 0.00170	-0.12127	112.36 ± 1.57
		45	0.23		[0.00][b]				
63	Titan ringlet IER		77867.13 ± 0.09	1	17.39 ± 0.12	270.54 ± 0.34	22.57503 ± 0.00082	0.01192	-11.13 ± 0.77
		86	0.62		[0.00][b]				
				0	3.84 ± 0.10	40.93 ± 1.79	1391.16334 ± 0.00400	-0.14413	5.45 ± 0.15
				-5	0.45 ± 0.11	60.87 ± 2.81	1692.06574 ± 0.00714	-0.06973	2.13 ± 0.22
				-2	0.77 ± 0.11	30.21 ± 4.10	2109.40889 ± 0.01063	-0.11882	2.92 ± 0.26
62	Titan ringlet OER		77890.21 ± 0.14	1	27.20 ± 0.18	270.70 ± 0.32	22.57562 ± 0.00077	0.03719	-34.78 ± 0.72
		89	0.94		[0.00][b]				
				2	1.55 ± 0.17	172.61 ± 3.05	717.94917 ± 0.00717	0.05868	-4.11 ± 0.50
				3	1.54 ± 0.17	110.60 ± 2.15	949.74161 ± 0.00517	0.06822	-3.65 ± 0.28
				4	0.90 ± 0.18	80.30 ± 2.51	1065.62338 ± 0.00602	0.05854	-2.80 ± 0.29
43	Colombo gap OEG		77926.01 ± 0.04	1	4.89 ± 0.05	280.02 ± 0.51	22.57696 ± 0.00118	0.07343	-68.79 ± 1.11
		75	0.27		[0.00][b]				

[a] The epoch is UTC 2008 January 1, 12:00:00.

[b] Quantities in square brackets were held fixed during orbit determination.

radial amplitude A_m, phase δ_m, and pattern speed Ω_p. Also listed are the difference between the fitted value of Ω_p and that predicted by Eq. (1), denoted by $\Delta\Omega_p$, and the corresponding radial offset. The latter is given by $\Delta a_p = \Delta\Omega_p/(d\Omega_p/da)$. (Note that the results given in the tables represent the final least-squares fit values, and differ slightly from those produced by the less-accurate spectral scanning program.)

The RMS residuals for the final fits, including the three normal modes on each edge, are 0.62 km for the inner edge and 0.94 km for the outer edge. Neither edge appears to show a significant inclination, and we have set $i = 0$ for the final fits.

Because of the significant difference in eccentricity between its inner and outer edges, the Titan ringlet exhibits a distinct width-radius relation, as shown in Fig. 5. In the upper panel we plot the individual radii for both edges, $\Delta r = r_i - \bar a$ and $r_o - \bar a$, as functions of $\cos f$, while in the lower panel we plot the actual measured widths as a function of the local mean radius, $\Delta\bar r = (r_i + r_o)/2 - \bar a$. (We use $\bar a$ to denote the mean semimajor axis of the inner and outer edges, and an upper-case Δ to denote departures from our best-fitting model or from a predicted value, as in $\Delta\Omega_p$ above.) For a narrow ringlet with edges given by keplerian ellipses whose elements differ by δa and δe, and assuming that the pericenters are aligned (*i.e.*, $\delta\varpi = 0$), the local radial width is given by

$$W(f) \approx \delta a - (\bar a\delta e + \bar e\delta a)\cos f = \delta a(1 - q\cos f), \tag{14}$$

where $q = \bar a\delta e/\delta a + \bar e$, so that, if $e \ll 1$ we have the linear relation

$$W(\Delta\bar r) \approx \delta a + \frac{\delta e}{\bar e}\Delta\bar r. \tag{15}$$

In both panels, the red lines indicate the radii and widths calculated from the best-fitting keplerian models for the two edges, while the green lines indicate the *envelope* of the radial variations associated with the normal modes we have identified. Note that the presence of the normal modes results in quite a large scatter in the width at any given value of the true anomaly or mean radius. From the fitted keplerian models, we calculate values for the mean width $\delta a = 23.1$ km, mean eccentricity $\bar e = 2.88 \times 10^{-4}$ and eccentricity gradient $q = 0.433$ that are used in Section 10 to update previous estimates of mass and surface density for this ringlet (Porco et al., 1984b).

In addition to the radial variations in the ringlet, Fig. 2 shows that both the inner and outer edges of the Colombo gap are also noticeably perturbed, with the distortions on the inner edge being opposite in phase from those of the ringlet and the outer edge. This is to be expected for resonantly-forced perturbations, since the resonant radius a_{res} falls within the gap but interior to the ringlet's centerline. In this situation, the *periapse* of the gap's inner edge is expected to be aligned with Titan, while the *apoapses* of the ringlet and outer gap edge are expected to track the satellite. Fits to both edges, also documented in Table 1, show that the forced eccentricity $A_1 \simeq 3.1$ km on the inner edge and 4.9 km on the outer edge, with pericenters that differ by 183° and pattern speeds consistent with Titan's mean motion of $22.5770^\circ\ \mathrm{d}^{-1}$.

6. Maxwell ringlet

Inhabiting the widest (~260 km) gap in the C ring at a mean radius of ~87,510 km, the Maxwell ringlet has long been considered to embody almost perfectly the paradigm of a freely-precessing eccentric ringlet (Esposito, 1983; Porco et al., 1984b). It also has the largest mean eccentricity of any Saturnian ringlet, with the exception of the F ring (Bosh et al., 2002), as well as a substantial eccentricity gradient q.

In Fig. 6 we plot the radii of both edges of the Maxwell ringlet vs their true anomalies, together with the keplerian fits listed in Table 2. The radial amplitude $ae = 18.9$ km on the inner edge and 58.0 km on the outer edge. The RMS residuals for both edges are remarkably small – 0.5 and 0.7 km, respectively – with almost all individual data points falling on the model curves at the scale of the figure. However, unlike the situation with the Titan ringlet, the best-fitting precession rates of the inner and outer edges of $14.69572 \pm 0.00022^\circ\ \mathrm{d}^{-1}$ and $14.69314 \pm 0.00005^\circ\ \mathrm{d}^{-1}$ differ by over 10 times the estimated uncertainty in the rate of the inner edge. If this difference had persisted for the past 30 years (the interval between the *Voyager* flybys and the latest *Cassini* data), then the pericenters of the inner and outer edges would now differ by almost 30°, which is at odds with the small but statistically-significant difference we find of $1.6 \pm 0.1^\circ$. The implication, therefore, is that the apsidal precession rates of the two edges may vary slightly relative to their long-term mean values. We will return to this possibility in Section 10. Further evidence for such variations comes from what appears to be a second $m = 1$ mode on the ringlet's inner edge with an amplitude $ae \simeq 0.6$ km and a slightly faster pattern speed. The beat period of the two $m = 1$ modes is ~11 year.

As in the case of the Titan ringlet, the deviations in the fitted precession rates from the local secular rates $\Delta\dot\varpi$ are best visualized in terms of the equivalent radial offsets, $\Delta a_{\dot\varpi}$. For the inner edge,

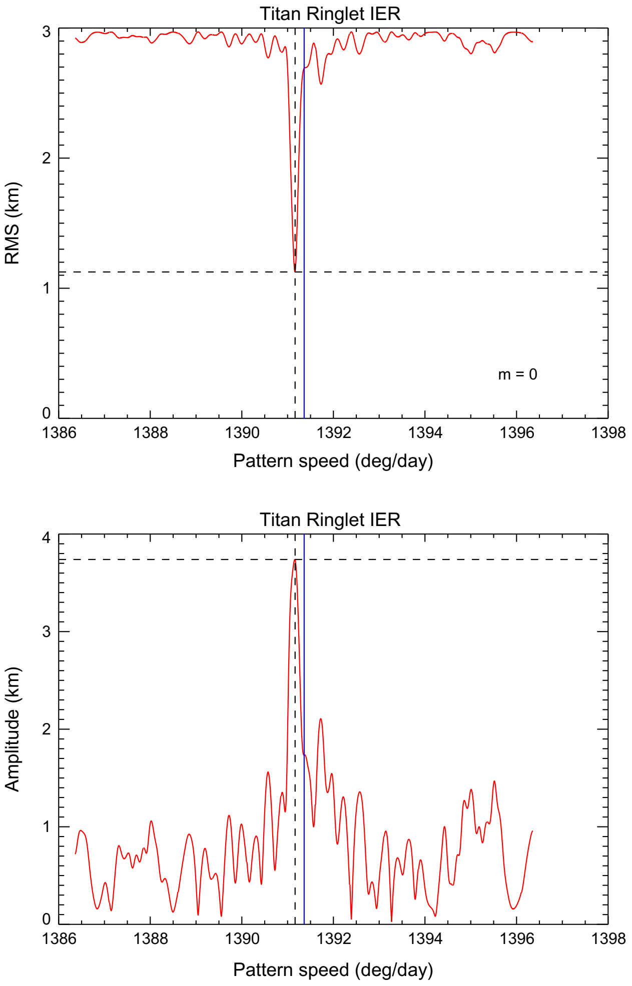

Fig. 4. A plot illustrating the discovery of an $m = 0$ normal mode on the inner edge of the Titan ringlet. The upper panel shows the RMS residual for the fits as the assumed pattern speed Ω_p is scanned across the predicted value for this feature, while the lower panel shows the corresponding radial amplitude A_0. The solid vertical line indicates the expected value of $\Omega_p = \kappa = 1391.361^\circ\ \mathrm{d}^{-1}$, while the dashed vertical line shows the rate that yields the best fit to the data: $1391.163^\circ\ \mathrm{d}^{-1}$. Horizontal dashed lines show the minimum residual of 1.13 km for $N = 89$ data points and the corresponding maximum amplitude of $A_0 = 3.74$ km.

$\Delta a_{\varpi} = +30.5$ km, whereas for the outer edge it is -24.3 km. In other words, the inner edge precesses at a rate appropriate to a semi-major axis of $a_i + \Delta a_{\varpi} = 87510.8$ km, while the outer edge precesses at a rate appropriate to a very similar semi-major axis of $a_o + \Delta a_{\varpi} = 87515.0$ km. These are quite close to the ringlet's geometric mean radius of $\bar{a} = 87509.8$ km. In Section 13 we discuss the constraint this result puts on the planet's zonal gravity harmonics.

Scanning for additional normal modes turns up nothing of significance on the inner edge, and only marginally-significant modes with $m = 2$ and $m = 4$ on the outer edge, with amplitudes of 0.2 and 0.3 km. Our overall post-fit RMS residuals for the inner and outer edges are 0.23 km and 0.16 km, respectively, which are among the lowest recorded for any noncircular feature we have studied and comparable to the best (circular) fiducial features.

Again, neither edge appears to show a significant inclination, and we have set $i = 0$ for the final fits.

As might be expected, given the very small normal mode amplitudes, the Maxwell ringlet exhibits an extremely clean width-radius relation, as shown in Fig. 7. Its mean width and eccentricity are $\delta a = 59.1$ km and $\bar{e} = 4.40 \times 10^{-4}$, and the average eccentricity

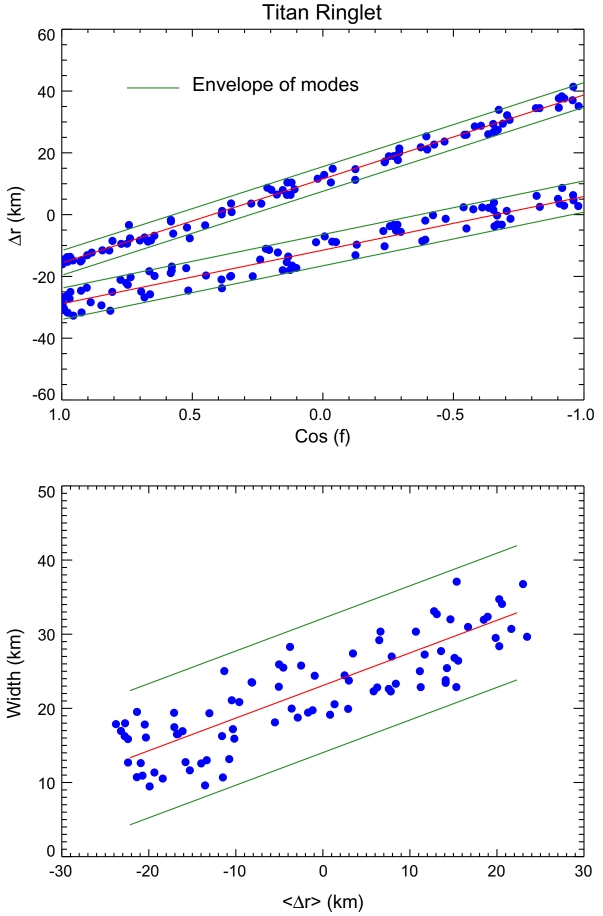

Fig. 5. The width-radius relation for the Titan ringlet. The upper panel shows the measured radii of both edges, relative to the mean semi-major axis of the inner and outer edges, $\bar{a}$, with red lines indicating the best-fitting keplerian ellipses. Green lines show the envelope of maximum variation for the normal modes on each edge. The lower panel shows the radial width of the ringlet, as a function of the local radius of its centerline $\bar{r}(\lambda, t) - \bar{a}$. Here the red line shows the mean width calculated from the keplerian fits to both edges, while the green lines again show the envelope of maximum variation due to the normal modes. (For interpretation of the references to color in this figure legend, the reader is referred to the web version of this article.)

gradient $q = 0.662$. There is almost no discernible deviation from the linear relation of Eq. (15). The minimum and maximum model widths are 19.98 and 98.16 km.

Although there is no strong satellite resonance within the Maxwell gap,[6] the outer edge of this gap is noticeably eccentric, like that of the Colombo gap. A keplerian fit to this edge, also presented in Table 2, reveals an amplitude $ae = 1.1$ km and a precession rate very similar to that of the nearby Maxwell ringlet but $0.056^\circ\ \mathrm{d}^{-1}$ faster than the predicted local value of $\dot{\varpi}_{\mathrm{sec}}$. The pericenter longitude differs by $171 \pm 3^\circ$ from that of the Maxwell ringlet. It thus seems very likely that the gap edge's eccentricity is in fact forced by that of the nearby ringlet, in a manner similar to that described by Borderies and Goldreich (1983) for a nearby satellite. A phase difference of $\sim 180^\circ$ between the pericenters of the two edges is quite consistent with this picture, inasmuch as the natural precession rate of the outer gap edge is slower than that of the ringlet, and the response of a simple harmonic oscillator to forcing at a frequency greater than its natural frequency is normally 180° out of phase with the forcing term. The inner edge of the Maxwell gap is less distinct than the

---

[6] The relatively-weak Atlas 2:1 ILR falls just exterior to the gap at 87646.9 km, where it drives a low-amplitude density wave (Baillié et al., 2011).

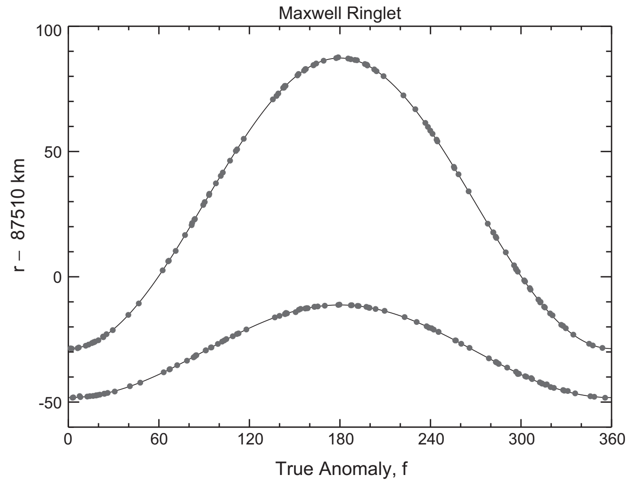

Fig. 6. Measured radii of the inner and outer edges of the Maxwell ringlet as functions of true anomaly. Solid lines show the best-fitting keplerian models derived separately for both edges.

outer edge, and our measurements show no detectable eccentricity above the RMS noise level of 0.4 km.

The Maxwell ringlet is not, however, without some surprises. In Fig. 8 we illustrate its internal structure, again using a series of optical depth profiles from VIMS occultations of the bright star γ Crucis. With an elevation angle of $B_* = 62.3°$, these are amongst the highest-SNR profiles available, and they show a puzzling wave-like pattern of peaks and troughs extending across much of the ringlet's width. The character of these oscillations seems to change systematically with true anomaly. Similar wavelike structure is seen in some, but not all, UVIS and RSS profiles, and in the highest-resolution ISS images (see Fig. 4a in Porco (2005)). This wave is currently the subject of investigation and will be the subject of a future paper.

7. Bond ringlet

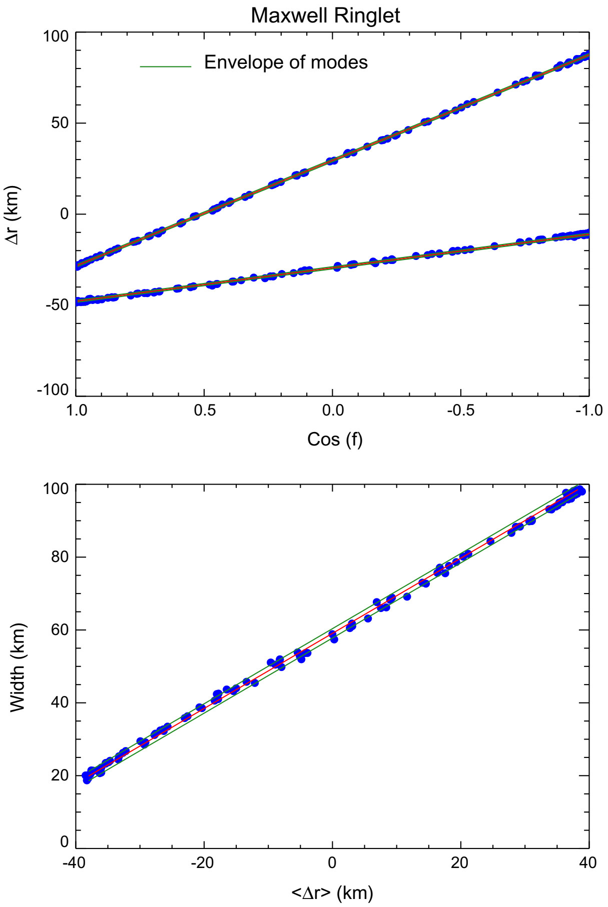

Fig. 7. The width-radius relation for the Maxwell ringlet. The upper panel shows the measured radii of both edges, relative to the mean semi-major axis of the inner and outer edges, $\bar{a}$, with red lines indicating the best-fitting keplerian ellipses. The lower panel shows the radial width of the ringlet, as a function of the local radius of its centerline $\bar{r}(\lambda, t) - \bar{a}$. Here the red line shows the mean width calculated from the keplerian fits to both edges. The green lines show the envelope of maximum variation due to the normal modes. (For interpretation of the references to color in this figure legend, the reader is referred to the web version of this article.)

In addition to the broad Maxwell gap, the outer C ring is home to two much narrower gaps, each of which is associated with a second-order resonance with Mimas. The first of these, 37 km wide and originally labeled by its approximate Saturnicentric distance of 1.47 R_S, is now known as the Bond gap. It is occupied by a narrow, sharp-edged ringlet with a mean radius of ~88,710 km and a width of ~17 km, whose optical depth is substantially higher than that of the surrounding material. The inner edge of this ringlet very nearly coincides with the Mimas 3:1 IVR at 88702.2 km, which might be expected to produce detectable vertical distortions, while the Prometheus 2:1 ILR at 88713.1 km falls near its centerline (see Fig. 11 in Nicholson et al. (1990)). A previous investigation by Porco and Nicholson (1987) produced evidence for radial variations in the ringlet edges of a few km, but no clear signature of resonant perturbations or a free eccentricity.

Table 2
Maxwell ringlet and gap orbital elements.

ID	Feature	N	a (km) rms (km)	m	ae (km) $a \sin i$ (km) A_m (km)	$\varpi_0(°)$[a] $\Omega_0(°)$ $\delta_m(°)$	$\dot{\varpi}(°/\mathrm{d})$ $\dot{\Omega}(°/\mathrm{d})$ $\Omega_p(°/\mathrm{d})$	$\Delta\dot{\varpi}(°/\mathrm{d})$ $\Delta\dot{\Omega}(°/\mathrm{d})$ $\Delta\Omega_p(°/\mathrm{d})$	$\Delta a_{\dot{\varpi}}$ (km) $\Delta a_{\dot{\Omega}}$ (km) Δa_p (km)
163	Maxwell gap IEG	102	87342.77 ± 0.05 0.43	1	[0.00][b] [0.00][b]				
61	Maxwell ringlet IER	105	87480.29 ± 0.02 0.23	1	18.93 ± 0.03 [0.00][b]	55.60 ± 0.10	14.69572 ± 0.00022	-0.01875	30.53 ± 0.36
60	Maxwell ringlet OER	105	87539.36 ± 0.02 0.16	1	58.02 ± 0.02 [0.00][b]	57.20 ± 0.02	14.69314 ± 0.00005	0.01488	-24.32 ± 0.09
				2	0.19 ± 0.03	73.26 ± 3.63	599.52336 ± 0.00823	0.08375	-7.95 ± 0.78
				4	0.29 ± 0.02	16.55 ± 1.22	891.94002 ± 0.00289	0.12007	-7.75 ± 0.19
164	Maxwell gap OEG	102	87610.12 ± 0.05 0.41	1	1.11 ± 0.06 [0.00][b]	228.54 ± 3.12	14.69150 ± 0.00716	0.05649	-92.63 ± 11.75

[a] The epoch is UTC 2008 January 1, 12:00:00.

[b] Quantities in square brackets were held fixed during orbit determination.

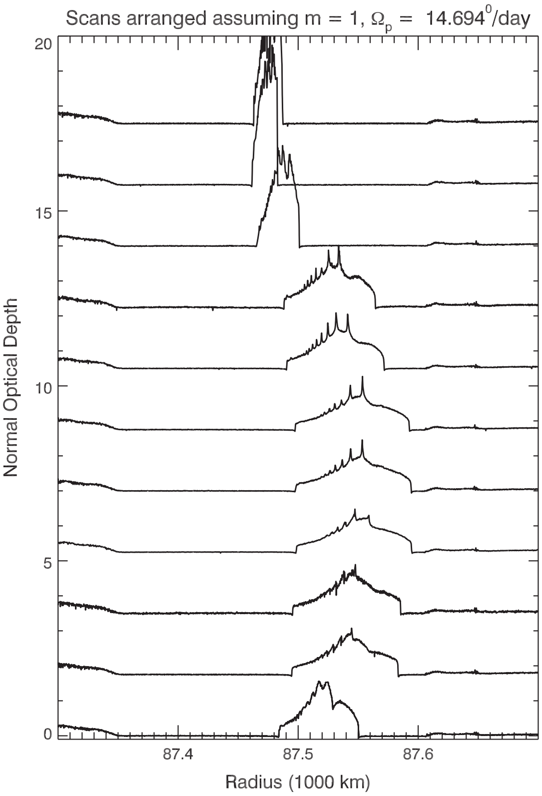

Fig. 8. A sequence of optical depth profiles of the Maxwell ringlet derived from eleven VIMS γ Cru occultations. The individual profiles are offset vertically and arranged in order of increasing true anomaly. At this scale both gap edges appear circular, but measurements of the outer edge, at 87,610 km, show that it has a small eccentricity that is out of phase with that of the ringlet (see text). Note the wavelike internal structure in the inner two-thirds of the ringlet.

Surprisingly, our 109 measurements of the inner edge show no obvious radial variations, and a simple keplerian fit yields very small radial and vertical amplitudes of $ae = 0.1$ km and $a \sin i = 0.2$ km, with RMS residuals of only 0.28 km. Given the presence of the Mimas IVR, we also carried out spectral scans to search for forced vertical distortions with $m = 2$. However, we find no evidence for the anticipated signature at pattern speeds near the predicted rate of 573.4750° d^{-1} (see Table 10 in Appendix A); our fits set an upper limit on the vertical amplitude of ~0.13 km, within a range of 10° d^{-1} centered on this value. For further discussion see Section 11.2 below.

In contrast to the inner edge, a remarkably rich set of modes is found on the outer edge of this ringlet, with $m = 2, 3, 4, 5, 6$ and 7. Strongest of these signatures is an $m = 2$ mode with an amplitude of ~1.1 km, as shown in Fig. 9. The indicated pattern speed is 587.289° d^{-1}, very close to that of the Prometheus 2:1 resonance, which is equal to the satellite's mean motion of 587.2852° d^{-1} (see Table 10). The predicted rate for an $m = 2$ normal mode at this radius is a slightly slower 587.224° d^{-1}. (Recall that resonantly-forced and normal mode distortions of an edge with the same value of m have almost the same pattern speeds.) Fig. 10 shows the Bond ringlet's outer edge as a function of $m = 2$ phase, after subtracting the higher-m modes discussed below; the resonant signature is seen here quite clearly, despite its amplitude of only ~1.1 km.

The mean radius of the Bond ringlet's outer edge is 88719.2 km, or 6.1 km exterior to the Prometheus 2:1 ILR. Despite this relatively-large separation, a check of the orientation of the $m = 2$ mode supports the hypothesis that this distortion is in fact forced by the Prometheus resonance: the longitude of minimum radius, $\delta_2 = 105.1 \pm 1.5°$ matches quite well the value of 112.9° predicted for orbits exterior to this resonance (see Appendix A). Geometrically, our fit implies that one of the apoapses of the $m = 2$ pattern lags ~8° behind the satellite.

RMS residuals from the $m = 2$ model of the Bond ringlet's outer edge remain substantial at ~0.7 km, which led us to carry out a search for additional normal modes. We find statistically-significant signatures for $m = 3$, 4, 5, 6 and 7, with amplitudes of 0.3–0.5 km. Our best overall fit for the outer edge is summarized in Table 3; the post-fit residual of 0.32 km is comparable to that of the inner edge, with mode amplitudes ranging from 0.30 km for $m = 5$ and 6 to 0.55 km for $m = 3$. We also find evidence for two very weak normal modes on the inner edge, with amplitudes of less than 0.2 km.

Note that, unlike the Titan and Maxwell ringlets, neither edge of the Bond ringlet shows a significant $m = 1$ perturbation, corresponding to a precessing keplerian ellipse. Nor do we find any evidence for a measurable inclination, with an upper limit on $a \sin i$ of ~0.3 km. A sequence of profiles derived from the VIMS γ Crucis occultations is shown in Fig. 11, arranged to illustrate the dominant $m = 2$ mode associated with the Prometheus 2:1 ILR.

Fits to both edges of the Bond gap show them to be circular, with RMS residuals of 0.76 km for the inner edge, which is rather indistinct and difficult to measure accurately, and 0.30 km for the outer edge.

With no appreciable eccentricity on either edge, the Bond ringlet does not have a conventional width–radius relation. As shown in the lower panel of Fig. 12, the small width variations that do exist are positively correlated with the mean radius, simply because both are controlled largely by the $m = 2$ perturbation on the outer edge.

8. Dawes gap and embedded ringlet

The outermost and narrowest of the three gaps in the outer C ring is located at ~90,210 km. Originally labeled by its approximate Saturnicentric distance of 1.495 R_S, it is now known as the Dawes gap. The gap itself is only ~20 km wide, but it is bordered on its inner edge by an unusually-opaque plateau-like feature, 62 km wide. This feature has previously been referred to as the 1.495 R_S ringlet, but it is not detached from the rest of the C ring and thus does not properly merit the term "ringlet." Colwell et al. (2009) refer to it as an embedded ringlet, and designate it as ER16. The inner edge of the Dawes gap (or the outer edge of the embedded ringlet) is quite sharp and nearly coincides with the Mimas 3:1 ILR at 90198.3 km. This is the second-strongest Lindblad resonance in the C ring[7] and is expected to produce detectable radial distortions. The much weaker Pandora 2:1 ILR falls at 90167.8 km, near the centerline of the embedded ringlet and ~30 km interior to the gap edge (see Fig. 11 in Nicholson et al. (1990)). A previous investigation of the ringlet by Porco and Nicholson (1987) produced strong evidence for radial variations on its outer edge (equivalent to the inner gap edge) of at least 10 km, but was unable to establish a convincing pattern consistent with either a free eccentricity or a forced perturbation due to the Mimas or Pandora ILR.

Our new measurements confirm the highly-variable nature of the inner gap edge. A simple keplerian least-squares fit yields a substantial eccentricity with an amplitude $ae = 5.4$ km, although we note that the best-fitting apsidal precession rate is 0.020° d^{-1} faster than predicted, corresponding to a radial offset of $\Delta a_{\varpi} = -37.9$ km, or about one-half the width of the ringlet. But this fit leaves unacceptably-large RMS residuals of ~4 km.

---

[7] The strongest is the Titan 1:0 apsidal resonance.

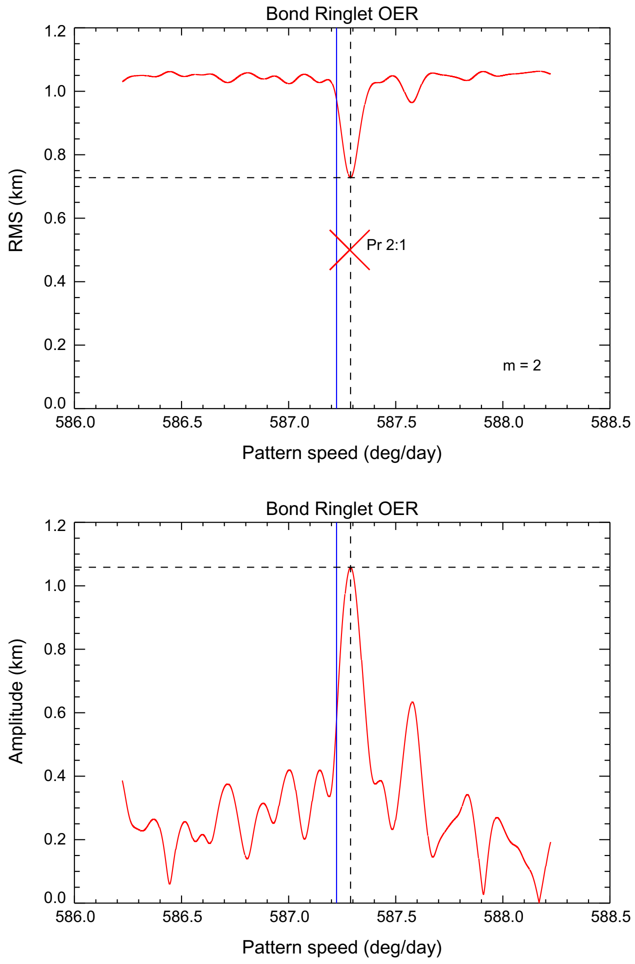

Fig. 9. A plot illustrating the $m = 2$ radial perturbation on the outer edge of the Bond ringlet. The upper panel shows the RMS residual for the fits as the assumed pattern speed Ω_p is scanned across the predicted value for this feature, while the lower panel shows the corresponding radial amplitude A_2. The solid vertical line indicates the expected normal mode value of $\Omega_p = 587.224^\circ\ \mathrm{d}^{-1}$, while the dashed vertical line shows the rate which yields the best fit to the data: $587.289^\circ\ \mathrm{d}^{-1}$. This perturbation is almost certainly due to the Prometheus 2:1 ILR, whose predicted pattern speed of $587.2852^\circ\ \mathrm{d}^{-1}$ is denoted by a large X. Horizontal dashed lines show the minimum residual of 0.73 km for $N = 110$ data points, and the corresponding maximum amplitude of $A_2 = 1.06$ km.

Scanning reveals an $m = 2$ pattern with $\Omega_p = 572.500^\circ\ \mathrm{d}^{-1}$ and an amplitude of ~5.2 km (see Fig. 13). The rate expected for a normal mode at this radius is $572.463^\circ\ \mathrm{d}^{-1}$ and the calculated pattern speed for the Mimas 3:1 ILR is $572.4749^\circ\ \mathrm{d}^{-1}$ (see Appendix A). So in this case, the observed pattern speed is significantly faster than *either* the free or forced frequency. (Note that secular perturbations from the relatively dense 1.495 R_S ringlet, or from the B ring, might modify the local apse rate, but these will not affect the Mimas pattern speed.) This unexpectedly rapid rate is confirmed by a least-squares fit, which yields $\Omega_p = 572.5054 \pm 0.0015^\circ\ \mathrm{d}^{-1}$; fixing the pattern speed at the resonant value leads to significantly larger residuals.

Despite these minor but puzzling discrepancies in the fitted pattern speeds, we find that the mean radius of the inner gap edge of 90200.4 km is within ~2 km of the resonant radius for the Mimas 3:1 ILR and that the $m = 2$ phase of $\delta_2 = 62.9 \pm 0.7^\circ$ closely matches the predicted value of 65.4° for orbits *interior* to this resonance.[8] On balance, therefore, we conclude that the $m = 2$ perturbation on the inner edge of the Dawes gap is indeed forced by the Mimas 3:1 ILR, but that this picture is likely to be incomplete. It is possible, for example, that the $m = 2$ pattern is librating about the equilibrium configuration with a period of several decades, as discussed in Section 12.3.

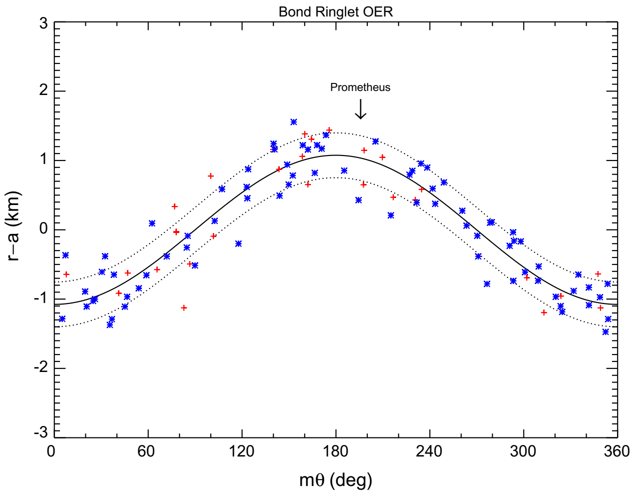

Fig. 10. Radial variations on the outer edge of the Bond ringlet, plotted vs $m = 2$ phase, $m\theta = 2[\lambda - \Omega_p(t - t_0) - \delta_2]$, after removal of the smaller normal modes listed in Table 3. Note that the apocenter is approximately aligned with Prometheus, as expected for orbits exterior to the 2:1 ILR, but lags by ~8°, as indicated by the arrow. In this figure, as well as in similar figures below, red crosses denote data from RSS occultations while blue asterisks indicate data from UVIS and VIMS stellar occultations. (For interpretation of the references to color in this figure legend, the reader is referred to the web version of this article.)

When both $m = 1$ and $m = 2$ modes are included, the RMS residuals for the inner edge of the Dawes gap are greatly reduced, but only to 1.6 km, suggesting that additional perturbations may be present. Indeed, further scans reveal evidence for two additional ILR-type normal modes on this edge, with $m = 3$ and 5 and amplitudes of 1.5 and 0.9 km, respectively. With all four components fitted, the RMS residuals are reduced to 0.75 km, as summarized in Table 4. The upper panel of Fig. 14 shows the radial residuals vs true anomaly, after removal of the $m = 2$, 3 and 5 perturbations, while the lower panel shows the residuals vs $m = 2$ phase, after removal of the $m = 1$, 3 and 5 perturbations.

A sequence of profiles derived from the VIMS γ Crucis occultations is shown in Fig. 15, arranged to illustrate the $m = 2$ mode associated with the Mimas 3:1 ILR. The seemingly-erratic variations that remain here are due to the large $m = 1$ (*i.e.*, keplerian) perturbations on this edge.

As in the case of the Maxwell gap, the outer edge of the Dawes gap also shows evidence of an eccentricity that may be sympathetically forced. A least-squares fit, reported in Table 4, yields an amplitude of $ae = 2.3 \pm 0.1$ km and a precession rate of $13.171^\circ\ \mathrm{d}^{-1}$ that is fairly close to that of the inner gap edge but much faster than the local apsidal rate at this radius (note that $\Delta\dot{\varpi} = +0.022^\circ\ \mathrm{d}^{-1}$, or $\Delta a_{\varpi} = -40.7$ km). The difference of $172 \pm 3^\circ$ between the pericenters of the two edges is also consistent with this suggestion, since the natural precession rate of the outer edge is less than the frequency at which it is being forced by the relatively massive ringlet at the inner edge.

Finally, we offer a few comments on the inner edge of the embedded ringlet at 1.495 R_S. A glance at Fig. 15 shows that this edge is much less sharp than the outer edge, with the optical depth decreasing gradually over ~10 km until it blends in with the background C ring. In this respect, the ringlet is more like a typical C ring plateau feature. Nevertheless, we have measured the half-light radius of this edge and carried out a standard keplerian fit. The

---

[8] It might be asked if this perturbation could instead be due to the weaker and more distant Pandora 2:1 ILR, but in this case the predicted pattern speed is much faster at $572.7886^\circ\ \mathrm{d}^{-1}$ and the expected $m = 2$ phase is 115.8°, both of which are far from the best-fitting values.

Table 3
Bond ringlet and gap orbital elements.

ID	Feature	N	a (km) rms (km)	m	ae (km) $a \sin i$ (km) A_m (km)	$\varpi_0\,(^\circ)$[a] $\Omega_0\,(^\circ)$ $\delta_m\,(^\circ)$	$\dot\varpi\,(^\circ/\mathrm{d})$ $\dot\Omega\,(^\circ/\mathrm{d})$ $\Omega_p\,(^\circ/\mathrm{d})$	$\Delta\dot\varpi\,(^\circ/\mathrm{d})$ $\Delta\dot\Omega\,(^\circ/\mathrm{d})$ $\Delta\Omega_p\,(^\circ/\mathrm{d})$	Δa_{ϖ} (km) $\Delta a_{\dot\Omega}$ (km) Δa_p (km)
111	Bond gap IEG		88686.01 ± 0.14	1	[0.00][b]				
		55	0.76		[0.00][b]				
59	Bond ringlet IER		88701.89 ± 0.03	1	[0.00][b]				
		109	0.28		[0.00][b]				
				0	0.17 ± 0.04	79.75 ± 13.61	1146.43579 ± 0.03378	-0.38569	20.08 ± 1.76
				3	0.16 ± 0.04	88.49 ± 4.60	778.35308 ± 0.01085	-0.18359	13.72 ± 0.81
58	Bond ringlet OER		88719.24 ± 0.04	1	[0.00][b]				
		106	0.32		[0.00][b]				
				2	1.08 ± 0.05	105.07 ± 1.48	587.29003 ± 0.00333	0.06685	-6.57 ± 0.33
				3	0.55 ± 0.06	107.67 ± 1.85	778.34105 ± 0.00450	0.03649	-2.73 ± 0.34
				4	0.47 ± 0.05	40.22 ± 1.75	873.86707 ± 0.00421	0.02182	-1.46 ± 0.28
				5	0.30 ± 0.06	52.06 ± 1.91	931.20532 ± 0.00440	0.03566	-2.24 ± 0.28
				6	0.30 ± 0.06	30.39 ± 1.73	969.40781 ± 0.00413	0.02187	-1.32 ± 0.25
				7	0.41 ± 0.05	14.05 ± 1.16	996.70499 ± 0.00277	0.02171	-1.27 ± 0.16
110	Bond gap OEG		88723.04 ± 0.04	1	[0.00][b]				
		96	0.30		[0.00][b]				

[a] The epoch is UTC 2008 January 1, 12:00:00.

[b] Quantities in square brackets were held fixed during orbit determination.

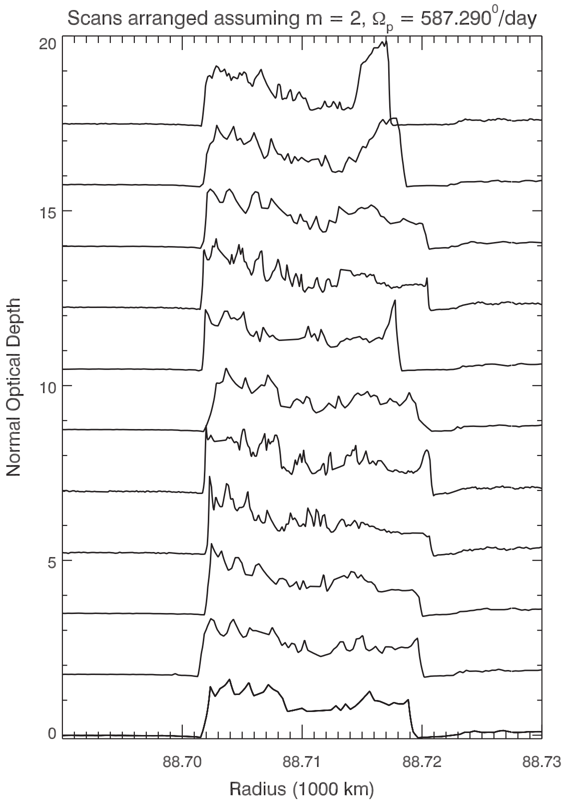

Fig. 11. A sequence of optical depth profiles of the Bond ringlet derived from eleven VIMS γ Cru occultations. The individual profiles are offset vertically and arranged in order of increasing $m = 2$ phase, using the best-fitting pattern speed. This amounts effectively to increasing longitude relative to Prometheus, modulo 180°. The inner edge of the ringlet appears to be circular, but measurements of the outer edge in Fig. 10 show that it has a radial amplitude of 1.08 ± 0.05 km, along with several additional normal modes. The outer gap edge at 88,723 km is circular, but quite hard to see at this scale.

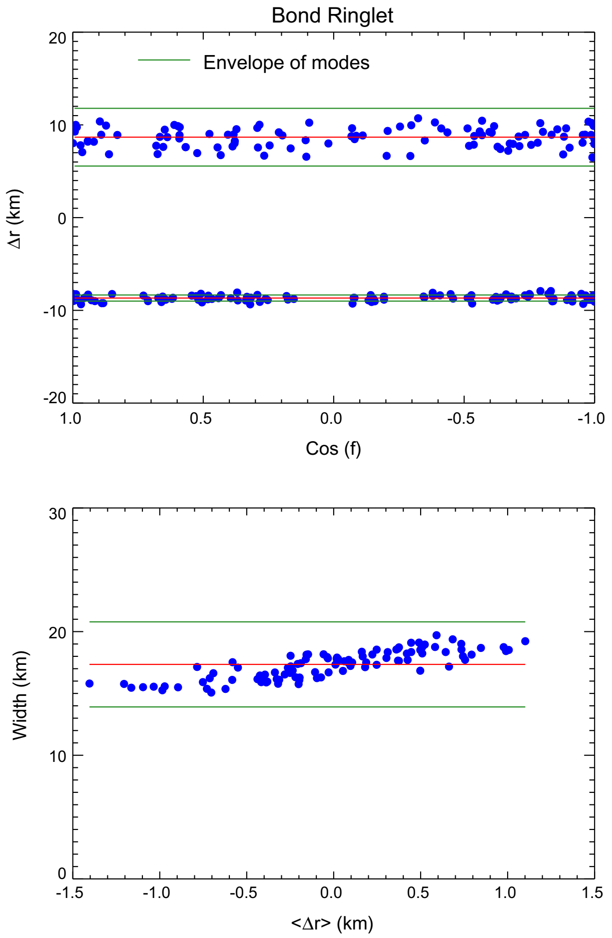

Fig. 12. A two-panel plot of Bond ringlet's width–radius relation, in the same format as Figs. 5 and 7. The weak correlation of width and mean radius results largely from their mutual dependence on the $m = 2$ perturbation acting on the outer edge of the ringlet.

results, also listed in Table 4, indicate a possible small eccentricity $ae = 1.4 \pm 0.1$ km. However, the precession rate of $13.229^\circ\,\mathrm{d}^{-1}$ is significantly faster than is expected at this radius.

We conclude by noting the small but consistent discrepancy between the fitted apsidal precession rates on all three edges measured in and near the Dawes gap and the rates predicted from Eq. (3) and Saturn's zonal gravity harmonics. Expressed in terms of the equivalent radial offsets Δa_{ϖ}, these are −67 km at the inner edge of the embedded ringlet, −38 km at the inner edge of the gap, and −41 km at the outer edge of the gap. We can offer no good

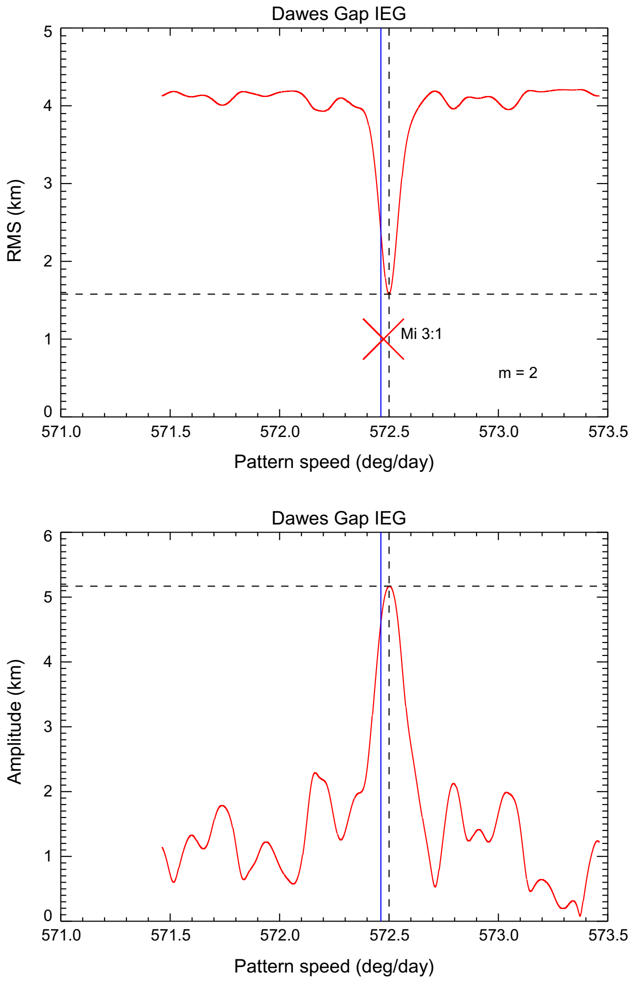

Fig. 13. A periodogram of the inner edge of the Dawes gap for $m = 2$, after removal of the $m = 1$ perturbation. The format is the same as that of Fig. 9. A strong peak with an amplitude of over 5 km is seen at a pattern speed of 572.500° d^{-1}, similar to but significantly faster than that of both the Mimas 3:1 ILR at 572.4749° d^{-1} – denoted by the large X – or that of an $m = 2$ normal mode at this radius (572.463° d^{-1}).

explanation for this, as the additional apsidal precession seems to be too large to attribute to secular perturbations from the B ring, even for a surface mass density above 100 g cm^{-2} (Nicholson and Porco, 1988; French et al., 2014a).

9. Other features

In addition to the four known gaps with narrow, embedded ringlets discussed above, we searched diligently for other noncircular features in the C ring that might have eluded previous studies. We identified and fitted nearly 80 additional features, including nearly 40 embedded ringlets, 22 plateau edges, and nine unnamed gap edges in the inner C ring. With the exception of ~25 features in the inner C ring that are detectably perturbed by the Titan 1:0 resonance (see Section 12.1 and Fig. 19 below), no additional noncircular features were found with radial amplitudes greater than ~0.5 km. Most of the newly-measured features have excellent orbit fits, with RMS residuals as low as 0.14 km. Three of the nine gap edges have RMS residuals below 0.20 km, and will serve as excellent benchmarks to establish the absolute radius scale of the inner C ring.

There are four very narrow gaps in the innermost C ring, between 74,535 km and 74,632 km, which we refer to informally as gaps A–D (visible but unlabeled in Fig. 1). In general, the interior edges of these gaps are quite sharp, with RMS residuals of ~0.15 km. However, the inner edge of gap B, at 74,588 km, is measurably inclined, with $a \sin i = 0.5$ km.

An exception to this pattern of sharp inner edges is provided by the heretofore unstudied gap at a radius of 75,728–75,807 km, labeled G1 by Colwell et al. (2009), which has a gradual and indistinct inner edge and a sharp *outer* edge (RMS residuals of 0.26 km and 0.17 km, respectively). The latter shows only a forced $m = 1$ perturbation due to the Titan 1:0 resonance with an amplitude of 0.18 km.

Among the most distinctive and prominent features in the C ring are the 11 plateau regions, designated P1 to P11 by Colwell et al. (2009) (see Fig. 1). The majority of these were listed as circular features by French (1993), and indeed we find that nearly all of the 22 plateau edges are highly circular, with typical RMS residuals below 0.20 km.

The C ring is also punctuated by a host of embedded ringlets. In addition to those previously enumerated by Colwell et al. (2009), we have identified and fitted nearly 20 others. Nearly all of these are also circular and equatorial, with RMS residuals ranging from 0.17 km to 0.7 km. An interesting exception is the ER8 ringlet at 77,650 km, just inside the Colombo gap. Appearing in our data set as two peaks separated by ~6 km, the inner and outer components show rather large forced $m = 1$ Titan perturbations with amplitudes of 1.75 km and 1.81 km, plus additional free $m = 1$ modes of 0.45 km and 0.23 km and inclinations $(a \sin i)$ of 0.36 and 0.30 km, respectively. The RMS residuals of the orbit fits are 0.21 km for the inner feature and 0.13 km for the outer feature.

10. Ringlet masses

Using the updated width–radius relations for the Titan and Maxwell ringlets shown in Figs. 5 and 7, we can revise the estimates for ringlet mass and mean surface density based on *Voyager* observations (Esposito, 1983; Porco et al., 1984b). The underlying model is that of Goldreich and Tremaine (1979), who postulated that the tendency of individual ring particle orbits in an eccentric ringlet to differentially precess under the influence of an oblate planet's gravity field is counteracted by gravitational interactions within the ringlet. This model requires that the outer edge of the ringlet be more eccentric than the inner edge, and the required mass is proportional to the planet's gravitational quadrupole moment J_2 and inversely proportional to the average eccentricity gradient $q \simeq a\delta e/\delta a$. Mass estimates based on this model have also been published for the Uranian α, β, δ and ϵ rings (Nicholson and Matthews, 1983; French et al., 1986, 1988b).

For simplicity, and following previous work, we use the analytic expression for the ringlet mass derived by Borderies et al. (1983), who divided the ringlet into two interacting streamlines. In units of the planet's mass M, the total ring mass is given by

$$\frac{M_r}{M} \approx \frac{21\pi}{16} J_2 \left(\frac{R}{a}\right)^2 \left(\frac{\delta a}{a}\right)^3 \left(\frac{e}{\delta e}\right) H(q)^{-1}, \tag{16}$$

where the dimensionless factor H is given by

$$H(q) = \frac{1 - \sqrt{1 - q^2}}{q^2 \sqrt{1 - q^2}}. \tag{17}$$

Although more complex models have been developed, in which the ring is divided into as many as 80 separate streamlines (Goldreich and Tremaine, 1979; Marouf et al., 1987), the resulting mass estimates differ by less than 50% from that given by Eq. (16).

Our results are given in Table 5, using the model parameters from Tables 1 and 2. In addition to the ringlet masses, we list the mean surface mass densities, $\Sigma = M_r/(2\pi a\delta a)$. For comparison,

Table 4
Dawes ringlet and gap orbital elements.

ID	Feature	a (km) N	rms (km)	m	ae (km) $a \sin i$ (km) A_m (km)	$\varpi_0(^\circ)$[a] $\Omega_0(^\circ)$ $\delta_m(^\circ)$	$\dot{\varpi}(^\circ/\mathrm{d})$ $\dot{\Omega}(^\circ/\mathrm{d})$ $\Omega_p(^\circ/\mathrm{d})$	$\Delta\dot{\varpi}(^\circ/\mathrm{d})$ $\Delta\dot{\Omega}(^\circ/\mathrm{d})$ $\Delta\Omega_p(^\circ/\mathrm{d})$	Δa_{ϖ} (km) Δa_{Ω} (km) Δa_p (km)
57	Dawes ringlet IER	90137.87 ± 0.06		1	1.35 ± 0.08	88.38 ± 2.80	13.22898 ± 0.00630	0.03560	-66.79 ± 11.81
		109	0.50		[0.00][b]				
56	Dawes gap IEG	90200.38 ± 0.10		1	6.10 ± 0.12	69.24 ± 1.05	13.18027 ± 0.00239	0.02014	-37.92 ± 4.50
		112	0.75		[0.00][b]				
				2	5.27 ± 0.11	62.92 ± 0.67	572.50536 ± 0.00150	0.03448	-3.54 ± 0.15
				3	1.46 ± 0.11	41.67 ± 1.57	758.94278 ± 0.00342	0.03512	-2.74 ± 0.27
				5	0.89 ± 0.11	71.02 ± 1.47	908.10954 ± 0.00342	0.05245	-3.43 ± 0.22
112	Dawes gap OEG	90220.77 ± 0.07		1	2.29 ± 0.07	241.79 ± 1.63	13.17088 ± 0.00328	0.02158	-40.67 ± 6.18
		61	0.32		[0.00][b]				
				2	0.43 ± 0.06	157.21 ± 4.55	572.48458 ± 0.00853	0.21244	-21.80 ± 0.88

[a] The epoch is UTC 2008 January 1, 12:00:00.

[b] Quantities in square brackets were held fixed during orbit determination.

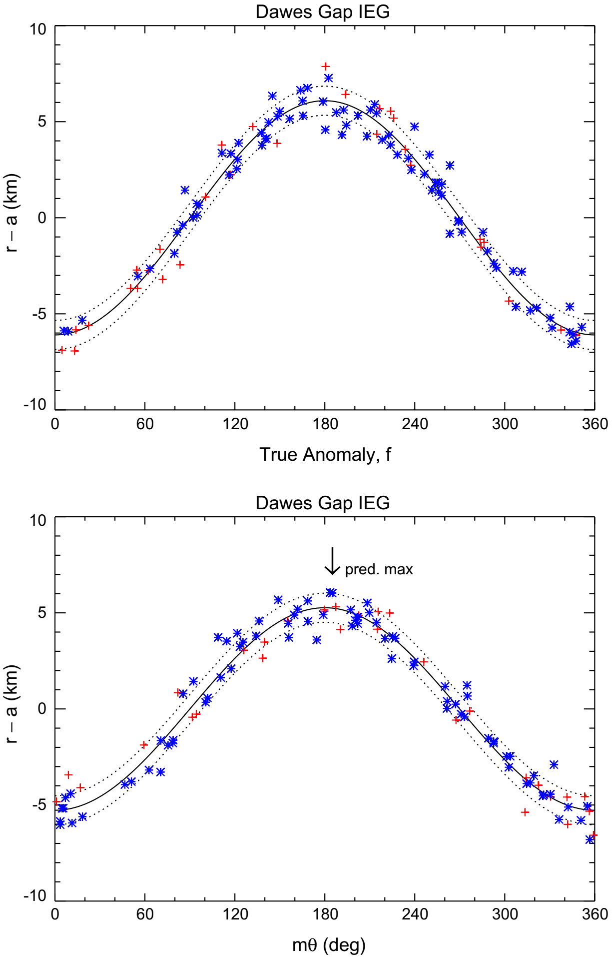

Fig. 14. Radial displacement of the inner edge of the Dawes gap vs true anomaly $\lambda - \varpi$ (top) and $m = 2$ phase $m\theta = 2[\lambda - \Omega_p(t - t_0) - \delta_2]$ (bottom), after subtracting the perturbations from two smaller modes listed in Table 4. Note the similar amplitudes of the two dominant perturbations, the second of which is attributed to the Mimas 3:1 ILR (see text). The maximum of the $m = 2$ pattern lags the predicted longitude by ~2.5°.

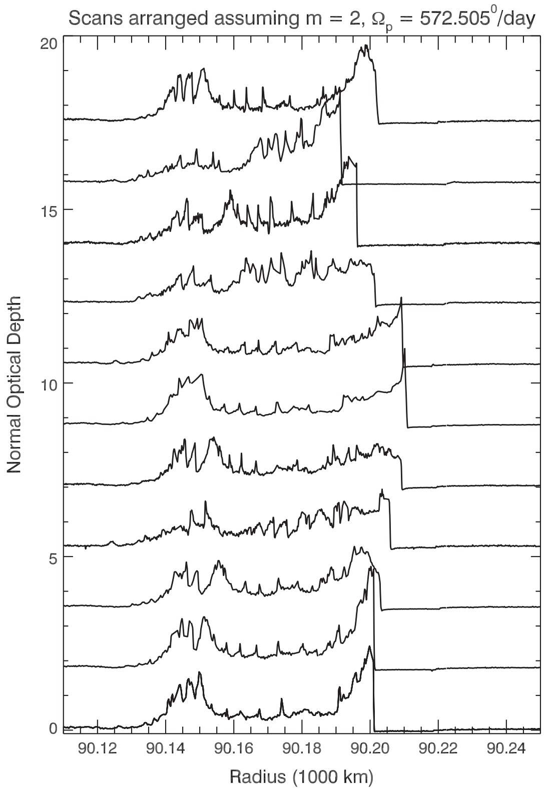

Fig. 15. A sequence of optical depth profiles of the Dawes gap and its associated embedded ringlet derived from eleven VIMS γ Cru occultations. The individual profiles are offset vertically and arranged in order of increasing $m = 2$ phase, using the best-fitting pattern speed. This highlights the forced perturbation of the inner gap edge due to the Mimas 3:1 ILR, shown in Fig. 14. Note that the outer edge of the gap at 90,221 km is also noticeably non-circular; our fits show a dominant $m = 1$ signature with a radial amplitude of 2.3 ± 0.1 km (see text).

we list the corresponding values for the Huygens ringlet and for the Uranian ϵ ring, using updated parameters from Paper III and French et al. (1991). All four rings yield surprisingly similar masses and very similar surface densities. The latter suggest average mass-weighted particle radii of $3\Sigma/4\rho\tau \simeq 20$ cm, assuming an internal density $\rho = 0.5$ g cm^{-3}, appropriate to porous water ice, and an average optical depth $\tau = 2$. The ringlet masses estimated in Table 5 are equivalent to spheres of such porous ice 18–26 km in diameter.

The derived surface densities of 20.3 and 22.2 g cm^{-2} for the Titan and Maxwell ringlets are consistent with previous estimates of 17 ± 5 g cm^{-2} (Porco et al., 1984b), and are roughly 4–10 times larger than the background C ring surface density determined from density waves (Baillié et al., 2011; Hedman and Nicholson, 2013). The ringlet values are comparable to the Uranian ϵ ring result of 25 g cm^{-2} (Goldreich and Tremaine, 1979), based on the latter's multi-streamline model. However, more recent theoretical models

Table 5
Ringlet masses derived from self-gravity models.

Ringlet	Titan	Maxwell	ϵ ring[a]	Huygens[b]
$\bar{a}$ (km)	77,879	87,510	51,149	117,814
$\bar{a}\bar{e}$ (km)	22.4	38.5	404.0	28.4
δa (km)	23.1	59.1	58.1	18.5
$q = a\delta e/\delta a$	0.433	0.662	0.651	0.022
$H(q)$	0.583	0.762	0.748	0.50
$M_r/M(10^{-11})$	0.40	1.27	7.57	0.97
M_r (10^{15} kg)	2.30	7.23	6.57	5.51
Σ (g cm^{-2})	20.3	22.2	35.2	40.2

[a] Based on data from French et al. (1991).
[b] Based on data from French et al. (2014a).

that include collisional as well as gravitational interactions between the ring particles suggest that the above simple calculation may significantly underestimate the true surface mass density (Chiang and Goldreich, 2000), so the actual numerical values in Table 5 should be treated with caution.

The above discussion implicitly assumes that the pericenters of the inner and outer ringlet edges are aligned, *i.e.*, that $\delta\varpi = 0$. In reality, dissipative forces within the ring, associated with inelastic collisions between the ring particles, are expected to result in a phase lag across the ring, with $\delta\varpi = \varpi_o - \varpi_i < 0$ (Borderies et al., 1983). Such phase lags have been measured for the Uranian α and β rings (Nicholson and Matthews, 1983), although this issue has not been revisited using the full set of available Uranian ring data. Our results show no significant phase lag for the Titan ringlet, with $\delta\varpi = 0.16 \pm 0.5^\circ$, and a small *phase lead* across the wider Maxwell ringlet of $\delta\varpi = +1.6 \pm 0.1^\circ$. The latter, together with the small but statistically significant difference in $\dot{\varpi}$ between the inner and outer edges (see Table 2), suggests instead that the Maxwell ringlet may be internally librating about an equilibrium configuration, as contemplated by Longaretti and Rappaport (1995). We will leave the interpretation of these results to future work.

11. Normal mode frequencies and amplitudes

The amplitudes of the free normal modes we have identified on the edges of the noncircular ringlets in the C ring are summarized in Figs. 16 and 17. Their distribution is remarkably consistent with the theoretical picture outlined in Section 2. As expected, we find ILR-type modes on the outer edges of ringlets and the inner edges of gaps (where density waves can propagate outwards from the ILR towards the sharp edge) and OLR-type modes on the inner edges of ringlets and the outer edges of gaps (where density waves can propagate inwards from the OLR). In general, although not invariably, we find that the mode amplitude decreases with increasing $|m|$ for any particular edge.

On the inner edge of the Titan ringlet we find OLR-type modes with $m = 0,\ -2$ and -5, while on the outer edge we find ILR-type modes with $m = 2$, 3 and 4. For the Maxwell ringlet we find weak ILR-type modes on the outer edge with $m = 2$ and 4. For the Bond ringlet we again find ILR-type modes on the outer edge, with $m = 3$, 4, 5, 6 and 7, as well as the $m = 2$ perturbation due to the Prometheus 2:1 resonance, and a very weak $m = 0$ OLR-type mode on the inner edge. Finally, at the inner edge of the Dawes gap we find unforced ILR-type modes with $m = 3$ and 5, as well as the $m = 2$ perturbation due to the Mimas 3:1 resonance.

The only apparent exceptions to this pattern are a very weak $m = 3$ ILR-type mode seen on the *inner* edge of the Bond ringlet and a weak $m = 2$ ILR-type mode on the *outer* edge of the Dawes gap. With an amplitude of only 160 m and a pattern speed equal to that of the $m = 3$ mode on the ringlet's outer edge, the former probably represents the evanescent tail of the much stronger outer edge mode (see Table 3), attenuated across the ringlet's width of 17 km. (Note that for this mode, $\Delta a_p = +13.7$ km, confirming that it is actually associated with the ringlet's outer edge, as expected.) The latter is discussed in Section 11.3 below and is likely to be a forced response to the strong but distant Mimas 3:1 ILR.

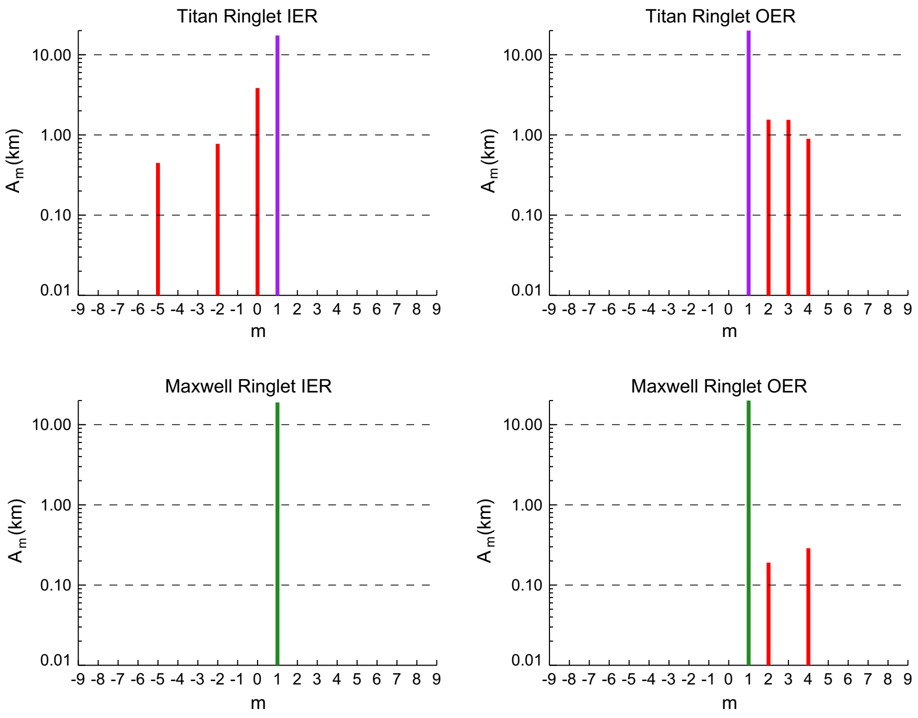

Fig. 16. A histogram of normal mode amplitudes for the inner and outer edges of the Titan and Maxwell ringlets. The left column shows inner ringlet edges while the right column shows outer ringlet edges. Positive values of m indicate ILR-type modes and negative values (or 0) indicate OLR-type modes. Red bars indicate free or normal modes, purple denotes resonantly-forced perturbations, and green denotes unforced $m = 1$ keplerian perturbations.

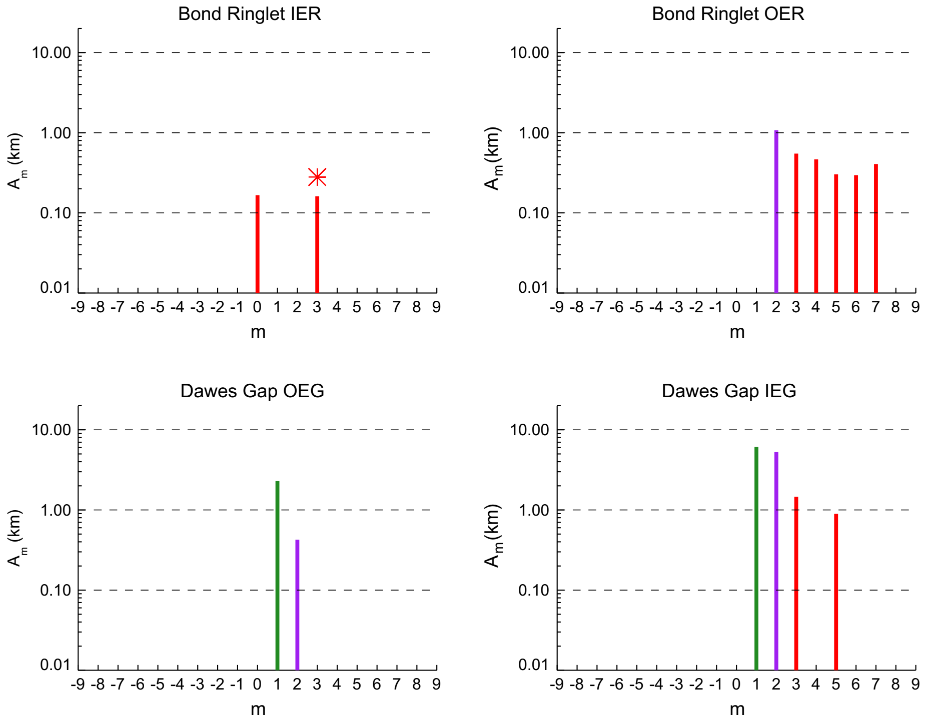

Fig. 17. A histogram of normal mode amplitudes for the inner and outer edges of the Bond ringlet and Dawes gap. The left column shows inner ringlet edges or outer gap edges, while the right column shows outer ringlet edges or inner gap edges. Positive values of m indicate ILR-type modes and negative values (or 0) indicate OLR-type modes. Red bars indicate free or normal modes, purple denotes resonantly-forced perturbations, and green denotes $m = 1$ keplerian perturbations. An asterisk calls attention to the anomalous ILR-type $m = 3$ mode on the inner edge of the Bond ringlet, which we attribute to the evanescent tail of the mode on the outer edge (see text).

In addition to the ILR/OLR mode dichotomy between outer and inner ringlet edges, the resonant cavity model outlined in Section 2 implies that in order to reflect the leading density wave, the resonant radii for each mode must lie within the ring material, rather than in the adjacent gap. For inner edges of ringlets (or outer edges of gaps), we thus expect that $a_{\rm res} > a_{\rm edge}$, while for outer edges of ringlets (or inner edges of gaps), we expect that $a_{\rm res} < a_{\rm edge}$. The final column in Tables 1–4 lists the separation, $\Delta a_p = a_{\rm res} - a_{\rm edge}$ for each identified mode, calculated from the best-fitting and predicted pattern speeds using

$$\Delta a_p = \frac{\Omega_p(\text{obs}) - \Omega_p(\text{pred})}{d\Omega_p/da}. \tag{18}$$

In this expression, the *predicted* pattern speed is computed from Eq. (1), using the best-fit value for the mean radius of the edge. Since $d\Omega_p/da < 0$ in all cases considered here, a positive value of Δa_p indicates that the observed pattern speed is *less* than that predicted at the ring edge, and thus that the corresponding resonant radius is *exterior* to the edge in question.

The calculated values of Δa_p are plotted for individual edges in Fig. 18, as a function of the value of m. (We have omitted those edges with no or very weak modes.) As predicted by the model, we find that Δa_p is positive for the OLR-type modes on the inner edge of the Titan ringlet, and negative for all ILR-type modes on the outer edges of the Titan and Bond ringlets, as well as the inner edge of the Dawes gap. Furthermore, the absolute value of Δa_p generally decreases with increasing $|m|$, which is consistent with the fact that, for a given surface mass density, the wavelength of density waves scales as $(|m-1|)^{-1}$ (Shu, 1984). To illustrate the trends, we have overplotted curves of $\Delta a_p = -9/|m-1|$ km and $\Delta a_p = -6/|m-1|$ km for the Titan ringlet IER and the Bond ringlet OER, respectively.

Based on the well-known dispersion relation for density waves, we can use the data in Fig. 18 to make a rough estimate of the surface mass density near the edges of the C ringlets. The method is the same as that outlined by Spitale and Porco (2010) and Nicholson et al. (2014) for the outer edge of the B ring, and amounts to assuming that the distance Δa_p between each mode's resonant radius and the ring edge is equal to 1/4 of the first wavelength of the corresponding density wave. Using Eq. (19) in Nicholson et al. (2014), which is based on the WKB approximation to the dispersion relation, and taking an amplitude-weighted average over all modes for a given edge, we obtain the mean surface densities listed in Table 6. Allowing for the observation that this simple formula underestimates the true surface density by about a factor of 4 (based on numerical simulations by P. Goldreich (personal communication, 2013) using the nonlinear density wave model of Borderies et al. (1986)), we find likely mass densities ranging from $7\ \mathrm{g\,cm^{-2}}$ for the Bond ringlet to $12\ \mathrm{g\,cm^{-2}}$ for the $1.495\ R_S$ ringlet and $\sim 24\ \mathrm{g\,cm^{-2}}$ for the Titan ringlet. The latter is quite similar to that obtained above from the self-gravity model, which provides further support for the validity of the resonant-cavity model.

We defer a more complete discussion of normal modes to Paper III, where we will present a much larger body of evidence for numerous ILR- and OLR-type modes on the edges of several narrow gaps and ringlets in the Cassini Division.

12. Resonant perturbations

In our study of noncircular features in the C ring, we have identified three instances where resonant perturbations by satellites appear to play a dominant role in shaping ringlet or gap edges. As summarized in Table 7, these are: (1) the Titan ringlet, both of whose eccentric edges precess at a rate which closely matches Titan's orbital mean motion; (2) the outer edge of the Bond ringlet,

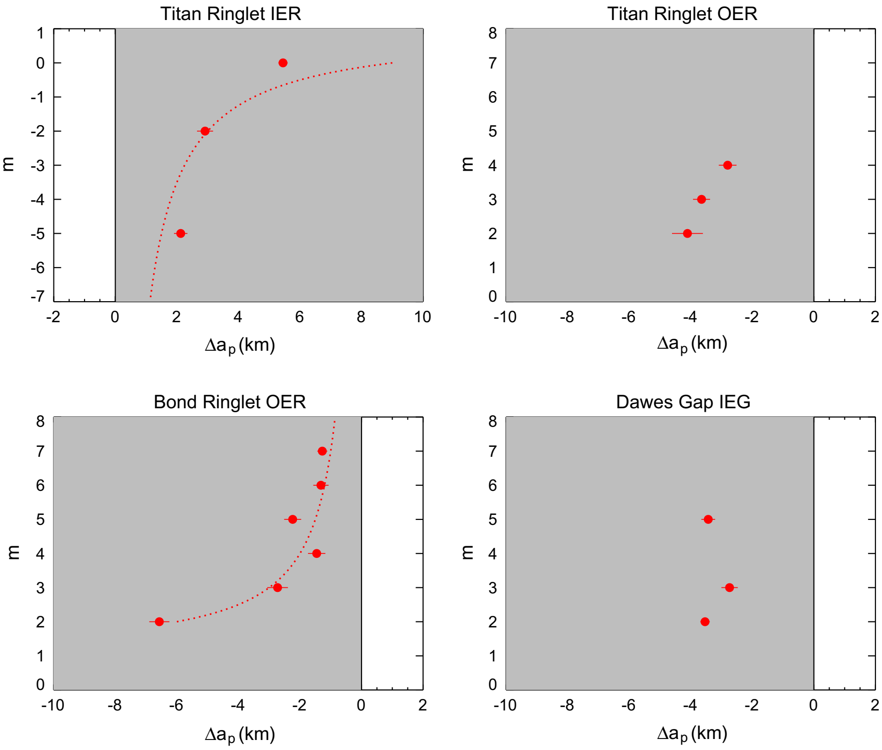

Fig. 18. The locations of calculated normal mode resonant radii relative to the corresponding ringlet and gap edges in the C ring. For each edge, the value of Δa_p is plotted vs m, with negative values of the latter indicating OLR-type modes. Vertical lines denote ringlet or gap edges, and shading indicates the presence of ring material. Resonantly-forced and $m = 1$ keplerian perturbations are excluded. Note that the magnitude of Δa_p generally decreases with increasing $|m|$, as illustrated by the overplotted curves $\Delta a_p = -9/|m-1|$ km and $\Delta a_p = -6/|m-1|$ km for the Titan ringlet IER and the Bond ringlet OER, respectively.

Table 6
Ringlet mass densities derived from normal modes.

Ring edge	Titan IER	Titan OER	Bond OER	Dawes IEG
a (km)	77,867	77,890	88,719	90,200
m values	0, −2, −5	2, 3, 4	3–7	3, 5
Σ (g cm^{-2})	6.5	5.2	1.7	3.0[a]

[a] The two modes give discrepant results of 2.0 & 6.1 g cm^{-2}.

Table 7
Resonant model fits.

Feature	Titan C/L[a]	Bond OER	Dawes IEG
Resonance	Titan 1:0 ILR	Prom. 2:1 ILR	Mimas 3:1 ILR
m	1	2	2
a (km)	77878.7 ± 0.15	88719.2 ± 0.1	90200.4 ± 0.1
A_m (km)	22.30 ± 0.15	1.08 ± 0.05	5.26 ± 0.11
Ω_p (° d^{-1})	22.5753 ± 0.0008	587.290 ± 0.003	572.5054 ± 0.0015
δ_m (°)[b]	270.62 ± 0.3	105.1 ± 1.5	62.9 ± 0.6
$\Delta a_{\rm res}$ (km)	-21.3 ± 0.15	-6.1 ± 0.1	-2.1 ± 0.1
$\Delta\Omega_p$ (° d^{-1})	-0.0017 ± 0.0008	0.005 ± 0.003	0.0305 ± 0.0015
$\Delta\delta_m$ (°)	-6.9 ± 0.3	-7.8 ± 1.5	-2.5 ± 0.6
$A_{\rm pred}$ (km)	18.1	0.3	3.8

[a] Centerline of ringlet: mean of fitted values for inner & outer edges.
[b] At epoch 2008 January 1, 12:00 UTC = JD 2454467.0.

which shows a small but significant $m = 2$ distortion rotating with Prometheus; and (3) the inner edge of the Dawes gap, which shows a much larger $m = 2$ distortion rotating at close to the rate predicted for the Mimas 3:1 ILR. In this section, we summarize the evidence for resonant forcing, compare the observed radial amplitudes with those predicted by theory, and examine several other weakly-perturbed nearby features.

In Table 7, we list for each feature the best-fitting semimajor axis a, resonant amplitude A_m, pattern speed Ω_p, and phase δ_m. Also listed are the corresponding differences between the observed and predicted pattern speeds $\Delta\Omega_p$ and orientations $\Delta\delta_m$, as well as the difference $\Delta a_{\rm res} = a_{\rm res} - a_{\rm fit}$ between the resonant radius and the mean fitted radius of the ring edge.[9] The predicted values are all taken from Table 10 in Appendix A. For the predicted phases, we have assumed that $\phi_L = 180°$ where the edges are clearly located exterior to the resonant radius (both Titan ringlet edges and the Bond ringlet's OER), and $\phi_L = 0°$ when most of the ringlet's mass is located interior to the resonant radius (Dawes gap inner edge).

The amplitudes of resonant perturbations are more difficult to predict with any accuracy than are the corresponding pattern speeds and phases. Not only are ring particles not the isolated test particles for which the expressions in Appendix A were derived, but even for an isolated object the predicted amplitude depends sensitively on its distance from the exact resonant radius $a_{\rm res}$. Within the context of the test particle model (see, for example, Section 10.3.2 of Murray and Dermott (1999)), the predicted amplitude is given by $A_m \approx \mathcal{S}/|a - a_{\rm res}|$, where the resonance strength $\mathcal{S}$ is determined by the mass and orbital elements of the perturbing satellite. For the resonances in question, numerical values of $\mathcal{S}$ are given in Table 10, based on expressions from Porco and Nicholson (1987) and Nicholson and Porco (1988), updated to reflect current estimates of the satellite masses (Jacobson et al., 2008b). Using these strengths, together with the observed values of $\Delta a_{\rm res}$, we calculate the predicted amplitudes listed in the last row of Table 7.

---

[9] This is deliberately defined in the same manner as Δa_{ϖ} and Δa_p above, in that it is the amount by which the calculated resonant radius is offset from the observed radius of the edge.

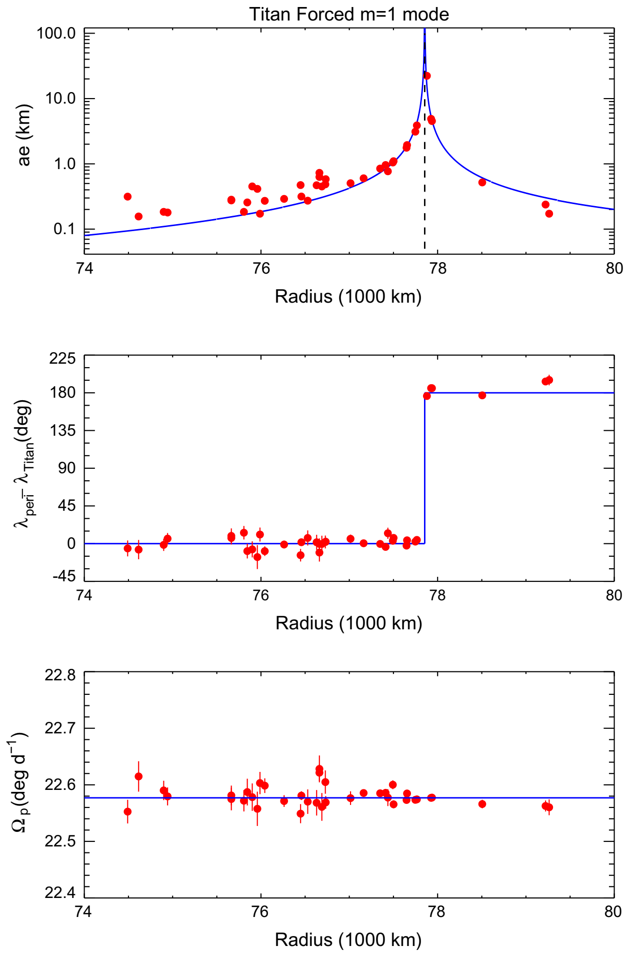

Fig. 19. Fitted amplitudes, phases and pattern speeds vs radius for $m = 1$ perturbations induced at a distance by the strong Titan 1:0 ILR. The curve in the upper panel shows the predicted amplitude, based on a simple test-particle model and the calculated resonance strength $\mathcal{S} = 382$ km^2 (see Table 10). The middle panel shows the phase of the perturbation relative to Titan; note that the orientation changes by 180° from inside to outside the resonant radius, in accord with the same model. The lower panel shows the best-fitting pattern speed Ω_p compared to Titan's mean motion of 22.577° d^{-1}.

12.1. Titan ringlet

In agreement with previous studies (Porco et al., 1984b; Nicholson and Porco, 1988; Melita and Papaloizou, 2005), we find that both edges of the eccentric Titan ringlet are effectively locked to the mean longitude of Titan. As expected for orbits exterior to the resonant radius, the apoapse of the ringlet is aligned with the satellite, with a small phase lag of 7°. This lag could plausibly represent either an equilibrium offset due to viscous dissipation within the ringlet, or a libration of the ringlet's orientation with respect to its mean orientation. One might hope to detect directly any such a libration in the *Cassini* data, but as its anticipated period is ~50 years (Nicholson and Porco, 1988), a much longer baseline of observations will probably be required. The mean best-fitting pattern speed of the inner and outer edges is $22.5753 \pm 0.0008°$ d^{-1}, or only 2σ away from the mean motion of Titan, which together with the small phase lag argues against a significant libration.

Given the strength of the Titan 1:0 apsidal resonance, which is comparable to that of the Mimas 2:1 ILR at the outer edge of the B ring (Hedman et al., 2010), its influence might be expected to be detectable over a significant radial range. Indeed, we have already noted in Fig. 2 that both the inner and outer edges of the Colombo gap show distinct $m = 1$ perturbations, apparently locked to the orbital longitude of Titan. The apoapse of the outer edge is approximately aligned with Titan (*i.e.*, $\phi_L = 180°$), as expected for orbits exterior to the resonant radius, as is the periapse of the inner edge (*i.e.*, $\phi_L = 0°$), which is located interior to $a_{\rm res}$.

Indeed, we find that similar forced perturbations are detectable in more than two dozen other features located throughout the inner C ring, and as much as 3500 km from the resonance. Fig. 19 shows the amplitude and phase of these forced eccentricities vs the radial location of the corresponding features. The measured amplitudes $A_1 = ae$ compare well with those predicted using the theoretical resonant strength, $\mathcal{S}$. All measured phases are consistent with $\phi_L = 0°$ for radii less than $a_{\rm res}$ and with $\phi_L = 180°$ for radii greater than $a_{\rm res}$, a strong indication that the measured eccentricities are real, despite their small sizes.

12.2. Bond ringlet

Unlike the Titan ringlet, where the observations seem to be largely in accord with theoretical expectations, the Bond ringlet remains something of an enigma. The first of the two resonances in this neighborhood is the Mimas 3:1 IVR, located within 0.3 km of the inner edge of the ringlet, but our attempts to find the anticipated $m = 2$ vertical distortion on this edge met with failure. Unlike radial distortions, vertical perturbations can be difficult to detect in occultation data, unless the inclination of the line of sight to the star (or Earth) with respect to the ring plane, usually denoted B_*, is small. But our *Cassini* data set contains 15 stellar occultations with $|B_*| < 30°$ and 5 with $|B_*| < 15°$, which should be quite sensitive to any vertical perturbations. It is possible that our sparse sampling does not cover the maximum vertical excursions, or that the vertical amplitude is simply too small to be detected in our data. At the observed mean radius of the inner edge, 88701.9 km, the predicted amplitude is $B_2 \approx \mathcal{S}/|a - a_{\rm res}| = 2.3$ km, although we note that an error of 1 km in the absolute radius scale could reduce this to ~0.5 km, which is more compatible with our upper limit. In contrast to the Titan 1:0 resonance, whose location is very sensitive to Saturn's higher-order zonal gravity harmonics (Nicholson and Porco, 1988), ordinary satellite resonances such as the Mimas 3:1 IVR can be readily calculated with sub-km accuracy.

The observed $m = 2$ perturbation on the outer edge, on the other hand, appears to be much larger than that expected to be produced by the Prometheus 2:1 ILR, though both the pattern speed and phase of the measured distortion match the resonant model well. In this case, the mean radius of the edge is 88719.2 km and $\Delta a_{\rm res} = -6.1$ km. Using the resonance strength from Table 10, we find a predicted amplitude of $A_2 \approx \mathcal{S}/|a - a_{\rm res}| = 0.3$ km, much less than our best-fit value of 1.08 ± 0.05 km. A possible answer to this puzzle was provided by Longaretti and Rappaport (1995), who found that a narrow ringlet can have a finite-amplitude equilibrium configuration, even in the absence of external forcing, if it is viscously overstable. In this case, the Prometheus resonance may simply provide a 'seed' $m = 2$ perturbation that subsequently grows to the equilibrium value (P-Y. Longaretti, private communication).

12.3. Dawes gap

As described in Section 8, the relatively-large $m = 2$ perturbation at the inner edge of the Dawes gap seems almost certainly to be due to the nearby Mimas 3:1 ILR, even though the fitted pattern speed is significantly faster than the expected value. The difference in Ω_p is $0.0305 \pm 0.0015°$ d^{-1}, or 20σ (see Table 7). In this case, we have $\Delta a_{\rm res} = -2.1$ km and the measured amplitude of 5.3 ± 0.1 km is in fairly good agreement with the test-particle model, which predicts that $A_2 \approx \mathcal{S}/|a - a_{\mathrm{res}}| = 3.8$ km. These results might be reconciled if the resonant argument, and thus the whole $m = 2$ pattern, is librating about its equilibrium value of $\phi_L = 0^\circ$. The libration period would be of order $2\pi/\Delta\Omega_p \approx 30$ year, making such a libration undetectable over the relatively short span of *Cassini* observations. A similar situation exists at the outer edge of the B ring with the much stronger Mimas 2:1 ILR, where the instantaneous amplitude of the $m = 2$ distortion varies from only a few km to over 70 km with a period of 5.4 year (Spitale and Porco, 2010; Nicholson et al., 2014).

We note for completeness that the weaker Pandora 2:1 ILR, which is located more than 30 km interior to the gap edge, should produce a perturbation at the inner gap edge of ~0.02 km, far too small to detect in the present data, and with a substantially faster pattern speed.

One might ask if, like the Titan 1:0 resonance, the influence of the Mimas resonance may also be seen further away from the resonant radius. In fact, our fit to the outer edge of the Dawes gap, which is located ~22 km exterior to the 3:1 resonance, does reveal a small $m = 2$ perturbation at the expected pattern speed (see Table 4). The phase $\delta_2 = 157 \pm 5^\circ$ is consistent with that expected for orbits exterior to the resonance (see Table 10), while the predicted amplitude $A_2 \approx \mathcal{S}/|a - a_{\mathrm{res}}| = 0.36$ km also matches the observed value of 0.43 ± 0.06 km.

13. Constraints on Saturn's zonal gravity harmonics

Our revised models for the Maxwell and Titan ringlets provide potentially-valuable constraints on Saturn's zonal gravity harmonics, $J_2,\ J_4,\ J_6$, etc. In the case of the freely-precessing Maxwell ringlet, this follows directly from comparing the observed apsidal precession rate with that calculated from Eq. (3), while for the resonantly-forced Titan ringlet the constraint is provided indirectly by comparing the observed eccentricity with that predicted by the resonance model described in Appendix A.

Looking first at the Maxwell ringlet, we recall from Section 6 that the best-fitting values of $\dot\varpi$ for the inner and outer edges are very similar (although not identical), with that of the inner edge corresponding to the predicted rate for a radius of $a_i + \Delta a_{\dot\varpi} = 87510.8 \pm 0.4$ km while that of the outer edge corresponds to that predicted for a radius of $a_o + \Delta a_{\dot\varpi} = 87515.0 \pm 0.1$ km. We may take the average of these two radii, weighted by the inverse of their uncertainties, 87514.2 km, as our best estimate of the dynamical "center of mass" of the Maxwell ringlet, which we denote by a(calc). (This result, of course, depends on our adopted set of Saturn's zonal gravity coefficients, derived by Jacobson et al. (2008a) and listed for convenience in Table 8.) This may be compared with the *observed* mean semi-major axis of the ringlet. To first order, this is given by the mean of the inner and outer edges, $\bar{a} = 87509.8 \pm 0.03$ km (see Table 2), but a better estimate is provided by the *average* semi-major axis, weighted by the normal optical-depth profile. Integrating several high-SNR VIMS profiles near quadrature, we find that $a(\mathrm{obs}) = 87512.4 \pm 0.1$ km.

The difference $\delta a = a(\mathrm{calc}) - a(\mathrm{obs}) = +1.8$ km is only marginally significant, given the adjustments to a(calc) and a(obs) made above, but may be attributable to small errors in the adopted values of Saturn's zonal gravity harmonics. Denoting the necessary corrections to J_2 by δJ_2, etc., and following the approach of Nicholson and Porco (1988), we may write the resulting constraint in algebraic form:

$$\frac{\partial\dot\varpi}{\partial a}\,\delta a = \sum_{n=1}^{\infty}\frac{\partial\dot\varpi}{\partial J_{2n}}\,\delta J_{2n}. \tag{19}$$

(The left hand side of this equation is simply $<\Delta\dot\varpi>$, the difference between the weighted average precession rate of the ringlet and that predicted to apply at its optical depth center.) The numerical values of the partial derivatives, based on expressions given by Nicholson and Porco (1988) and evaluated at $\bar{a}$, are listed in Table 9. For example, if we were to correct the predicted precession rates, and thus a(calc), by adjusting J_4 or J_6, while keeping the other zonal coefficients at their present values, we would need either $\delta J_4 = +1.1 \times 10^{-6}$ or $\delta J_6 = -1.3 \times 10^{-6}$.

Turning now to the Titan ringlet, we cannot use the fitted apsidal precession rate to constrain the harmonic coefficients, as this is set by Eq. (1) to be equal to the mean motion of Titan, n_T. However, if the libration amplitude of the ringlet is negligible, as we concluded in Section 11.1, then so is its free eccentricity and we may conclude that the observed eccentricity is entirely forced. In this situation, we may assume, as did Nicholson and Porco (1988), that the ringlet's *mean* eccentricity can be used to determine the distance of the ringlet's center of mass from the resonant radius a_{res}. For the center of mass radius, we use the average of the fitted semi-major axes for the inner and outer edges, $\bar{a} = 77878.7 \pm 0.15$ km (the very high optical depth of the Titan ringlet precludes calculating a weighted mean radius as we did for the Maxwell ringlet above). For the forced eccentricity we use the average of the fitted $m = 1$ amplitudes for both edges, $A_1 = 22.30 \pm 0.15$ km, as listed in Table 7.

Using the resonance strength from Table 10, and noting that the apoapse of the ringlet is aligned with Titan, we find that the deduced (or "observed") value of $\Delta a_{\mathrm{res}} = \mathcal{S}/A_1 = -17.1$ km. The estimated location of the apsidal resonance, based on the Titan ringlet's mean forced eccentricity, is thus $\bar{a} + \Delta a_{\mathrm{res}} = 77861.5 \pm 0.2$ km, where the quoted error bars reflect only our 1σ fit parameter uncertainties. Systematic uncertainties in the ring's absolute radius scale are likely to add an additional uncertainty of ~0.3 km (French et al., 2014b). (This may be compared with the previous estimate for the resonant radius by Nicholson and Porco (1988) of 77852 ± 13 km.

Table 8
Adopted values for Saturn's gravity field.[a]

Parameter	Value	Units
GM	37,931,208	km^3 s^{-2}
R[b]	60,330	km
J_2	16290.7	10^{-6}
J_4	−935.5	10^{-6}
J_6	90.4	10^{-6}
J_8	−10.0	10^{-6}
J_{10}	2.0	10^{-6}
J_{12}	−0.5	10^{-6}

[a] Values for GM and $J_2 - J_8$ from Jacobson et al. (2008a). Nominal values for J_{10} and J_{12} from Nicholson and Porco (1988).
[b] Equatorial reference radius.

Table 9
Ringlet sensitivities to Saturn's zonal gravity coefficients.[a]

Parameter	Titan ringlet	Maxwell ringlet
a_{res} or $\bar{a}$ (km)	77857.4	87509.8
$\partial\dot\varpi/\partial a$ (° d^{-1} km^{-1})	−0.001072	−0.000613
$\partial\dot\varpi/\partial J_2$ (° d^{-1})	1265.36	840.40
$\partial\dot\varpi/\partial J_4$ (° d^{-1})	−1905.88	−1001.06
$\partial\dot\varpi/\partial J_6$ (° d^{-1})	2005.31	833.50
$\partial\dot\varpi/\partial J_8$ (° d^{-1})	−1807.29	−594.53
$\partial\dot\varpi/\partial J_{10}$ (° d^{-1})	1492.70	388.65
$\partial\dot\varpi/\partial J_{12}$ (° d^{-1})	−1165.46	−240.19

[a] Based on gravity parameters from Jacobson et al. (2008a) and for a reference radius of 60,330 km.

Comparing this observed value with the *predicted* resonant radius in Table 10, calculated using the zonal gravity harmonics of Jacobson et al. (2008a), we find that $\delta a = a_{\rm res}({\rm calc}) - a_{\rm res}({\rm obs}) = -4.1 \pm 0.3$ km. (The fairly good agreement between the observed and predicted radii for the apsidal resonance is not, of course, completely unexpected inasmuch as Jacobson (2006) and Jacobson et al. (2008a) made use of a similar Titan ringlet constraint – based on Voyager data – published by Nicholson and Porco (1988) in their global solution for Saturn's gravity field.) The corresponding constraint on the zonal gravity coefficients is again given by Eq. (19), with the partial derivatives evaluated at $a_{\rm res}$ and listed in Table 9. Again as an example, if we were to match the resonant radius, and thus the forced eccentricity, by adjusting J_4 or J_6, while keeping all the other zonal coefficients at their present values, we would need either $\delta J_4 = -2.3 \times 10^{-6}$ or $\delta J_6 = +2.2 \times 10^{-6}$.

Although the corrections to the gravity field implied by our results for the Maxwell and Titan ringlets appear to be inconsistent, as indicated by the differing signs for δa, the magnitudes of the implied changes to J_4 and/or J_6 are small and comparable to the 1σ uncertainties quoted for the current gravity solution (Jacobson et al., 2008a) of ±1.0 and ±5.1, respectively, in units of 10^{-6}. It thus appears that very little adjustment to this solution is warranted by our results. We caution, however, that the estimates made in this section are rather crude. More refined calculations would take into account gravitational and viscous interactions within the Titan and Maxwell ringlets, which presumably act to enforce the observed state of uniform apsidal precession across each ringlet (Chiang and Goldreich, 2000; Melita and Papaloizou, 2005). Only then can the mean precession rate, or average forced eccentricity, be accurately linked to an effective mean semi-major axis. To reinforce this caution, we note that the Titan ringlet, in the absence of such internal forces, would be expected to have a *larger* eccentricity on its inner edge – which is closer to the apsidal resonance – than on its outer edge, *i.e.,* a negative eccentricity gradient, which is in violent disagreement with the observations. Unfortunately such a calculation is beyond the scope of this paper and must be deferred to a subsequent numerical study.

An improved set of zonal gravity coefficients should take into account not only the constraints provided by the Maxwell and Titan ringlets as well as all available spacecraft tracking data generated by the *Cassini* orbiter (Jacobson, 2006), and the observed precession rates of Saturn's natural satellites, but also any additional constraints from the rings. These may come from the apsidal precession of noncircular features in the D ring (Hedman, 2007; Hedman et al., 2014), as well as from the tightly-wound vertical corrugation identified there and in the C ring (Hedman et al., 2011). It is in order to facilitate such a future synthesis that we provide the updated ringlet constraints in Eq. (19) and Table 9. By leaving these in algebraic form, we allow for future refinements to the ringlet parameters as well as more realistic self-gravity models and the inclusion of presently unmodelled contributions to $\dot{\varpi}$, such as precession induced by nearby or distant ring material. (An estimate of the latter for the Titan ringlet of $0.0019^\circ\ {\rm d}^{-1}$ was made by Nicholson and Porco (1988).)

14. Conclusions

We have carried out a comprehensive survey of sharp-edged features in Saturn's C ring, using data from radio and stellar occultation experiments carried out by the *Cassini* spacecraft over a period of 5 years. Over 100 occultations are included in the combined data set, and up to 90 different features have been measured in each one. Our goal has been to identify and characterize all measurably noncircular features, with the ultimate aims of understanding the role played by satellite resonances in sculpting the C ring, and of increasing our understanding of the internal dynamics of narrow ringlets in general and their interactions with the gaps that harbor them.

14.1. Ringlet descriptions

As first noted by Esposito (1983), Porco et al. (1984b) and Porco and Nicholson (1987), the four prominent narrow gaps in the C ring each either contain a noncircular ringlet, or have one or more measurably noncircular edges. In some cases we find that these distortions are forced by nearby resonances with external satellites, but in others they represent either freely-precessing keplerian ellipses or more complex modes of oscillation, which we refer to as normal modes.

The Colombo gap in the inner C ring (77,750–77,925 km) contains a narrow, opaque and eccentric ringlet, generally known as the Titan ringlet, whose eccentricity appears to be primarily (or perhaps entirely) forced by the nearby Titan 1:0 (or apsidal) resonance. From its mean amplitude $ae = 22.3$ km, we calculate a revised radius for the apsidal resonance of 77861.5 ± 0.5 km, or 9 km greater than that adopted by Nicholson and Porco (1988) in their study of this ringlet in *Voyager* observations. In addition to the ringlet itself, we find evidence for resonantly-forced perturbations on both gap edges and on $\sim$25 other features as far as 3500 km from the resonance. Smaller perturbations on both inner and outer edges of the Titan ringlet are attributable to normal modes with wavenumbers $m = 0,\ -2$ and -5 on the inner edge and $m = 2,\ 3$ and 4 on the outer edge. Amplitudes range from 0.5 to 3.8 km.

The Maxwell ringlet, on the other hand, appears to be essentially a freely-precessing eccentric ringlet, with an amplitude that varies from 18.9 km on the inner edge to 58.0 km on the outer edge. It occupies the eponymous gap at 87,350–87,610 km and its edges exhibit only a few very low-amplitude normal modes. Although this ringlet is not influenced by any known satellite resonance, its internal density profile shows a systematic wavelike structure, which is the subject of a current investigation. The outer edge of the Maxwell gap shows a radial variation with an amplitude of $\sim$1 km that appears to be a forced eccentricity driven by its proximity to the ringlet.

Much narrower than either the Colombo or Maxwell gaps, the Bond gap at 88,686–88,723 km is half-filled by the sharp-edged and relatively opaque Bond ringlet. This ringlet has no measurable eccentricity (*i.e.,* an $m = 1$ perturbation), but its outer edge exhibits an $m = 2$ signature with an amplitude of 1.1 km that is evidently forced by the nearby Prometheus 2:1 inner Lindblad resonance, in addition to at least 5 weaker normal modes with $m = 3,\ 4,\ 5,\ 6$ and 7. To our surprise, we find no evidence for radial or out-of-plane distortions at the Bond ringlet's inner edge, despite its proximity to the Mimas 3:1 inner vertical resonance.

Outermost of the C ring gaps is the Dawes gap at 90,202–90,220 km, which is bounded on its inner edge by a 60 km-wide plateau-like structure but does not contain a conventional detached ringlet. The inner edge of the gap shows two large perturbations of comparable amplitude: an elliptical (*i.e.,* $m = 1$) signature with $ae = 6.1$ km and an $m = 2$ perturbation of amplitude 5.3 km. Although the latter is almost certainly driven by the nearby Mimas 3:1 ILR, to judge from its phase and amplitude, its pattern speed is significantly greater than predicted. Additional smaller perturbations reflect normal modes with $m = 3$ and 5. Like both the Colombo and Maxwell gaps, the outer edge of the Dawes gap shows what appears to be a small forced eccentricity, in this case due to the strongly-perturbed inner edge.

14.2. Normal mode summary

The identification of numerous normal modes co-existing on the sharp edges of ringlets and gaps is probably the most important new result of the present study. Although such modes had been seen in the very narrow Uranian γ and δ rings (French, 1988a), where they extend across the entire width of each ring, only the outer edge of the B ring has been previously known to exhibit what we may call "edge modes" (Spitale and Porco, 2010; Nicholson et al., 2014). The distribution of modes is in excellent agreement with theoretical predictions, with ILR-type modes on outer ringlet (and inner gap) edges and OLR-type modes on inner ringlet (and outer gap) edges, as illustrated in Figs. 16 and 17. Not at all clear, however, is what determines which particular modes will appear on any given edge, and what process sets their amplitudes. In general, there is a trend of decreasing amplitude with increasing azimuthal wavenumber m, but the limited data from the C ring do not permit further generalizations.

The exact pattern speed of a mode, which must satisfy Eq. (1), is set by the requirement that the corresponding inner or outer Lindblad resonance be located at distance from the ring edge Δa_p that permits a standing density wave to be established in the region between them. This is illustrated quite well in Fig. 18, where we also see that modes with larger values of $|m|$ generally have narrower resonant cavities. In particular, we note that no normal mode has been identified that has a resonant radius that falls in the gap beyond the ring material.

14.3. Self-gravity model & surface mass densities

Under the assumption that a ringlet's self-gravity is sufficient to counteract the expected differential apsidal precession of its inner and outer edges due to Saturn's oblateness, we have estimated the surface mass densities of the Titan and Maxwell ringlets from their average eccentricity gradients, determined from updated width-radius relations. We find $\Sigma = 20.3\ \mathrm{g\,cm^{-2}}$ for the Titan ringlet and $22.2\ \mathrm{g\,cm^{-2}}$ for the Maxwell ringlet, consistent with previous estimates based on both two streamline and multi-streamline models. More recent theoretical models suggest that these might substantially underestimate the actual surface density, but the similarity between the two values is notable.

14.4. Future directions for research

The precise kinematic models we have developed for the various noncircular ringlet and gap edges in the C ring should provide input and boundary conditions for more sophisticated models of narrow ringlet dynamics, such as that of Melita and Papaloizou (2005) and Hahn and Spitale (2013). Improved characterization of normal mode frequencies might provide a new method for estimating ring surface mass densities (Section 11), and perhaps even lead to insights into the mechanism by which the sharp edges of many ringlets and gaps are maintained against collisional diffusion.

The sheer abundance of normal modes on the edges of many (but by no means all) ringlet and gap edges is one of the most surprising results of this investigation, prompting questions about their excitation, amplitudes, and regional distribution. Hahn and Spitale (2013) have shown that normal modes, once present in a ring edge, have long persistence times, something that can be tested on the decadal timescale by extending the time baseline of the present study by including additional *Cassini* occultation observations.

Both the calculated radius of the Titan 1:0 ILR and the measured apsidal precession rate of the Maxwell ringlet provide improved constraints on the higher zonal harmonics of Saturn's gravity field, especially J_6 and J_8, but with some sensitivity through J_{12} and beyond (Nicholson and Porco, 1988; Jacobson, 2006). Combining these with measurements of other noncircular or inclined ring features should yield improved estimates of the gravity coefficients, compared to those derived from spacecraft tracking data alone.

Future *Cassini* occultation observations should permit refinements to the present models, especially to the fitted precession rates and pattern speeds, and the addition of *Voyager* and other pre-*Cassini* data for the Titan and Maxwell ringlets may lead to even better values.

A by-product of this work, to be explored in Paper IV, is the establishment of an accurate absolute radius scale for the rings, with residual errors likely to be at the 100 m level, and a definitive measurement of the precession rate of Saturn's pole. Present estimates of the latter (French, 1993; Jacobson et al., 2011) indicate a period of order 1.8 Myr, but a more accurate value would impose a significant constraint on the planet's polar moment of inertia and thus on its internal density distribution.

Acknowledgments

The occultation data we have relied on for this investigation would not have existed without the work of many dedicated individuals on the *Cassini* project, especially those on the RSS, UVIS and VIMS science and engineering teams. We also thank the dozens of "Team Cassini" undergraduate students at Wellesley College who assisted in the measurements of the thousands of individual ring features used in this study.

We would especially like to acknowledge several extensive discussions with Peter Goldreich, in the course of which we became much more familiar with the possibilities for normal modes on ring edges, and Pierre-Yves Longaretti for a particularly thorough and inciteful review.

This work was supported by NASA, through a grant to RGF from the Cassini Data Analysis Program.

Appendix A. Satellite resonances

In this section we provide some relevant theoretical background for the satellite resonances invoked in Sections 5–8, and collect the necessary numerical values in one place for easy reference. For more details on the calculation of resonance strengths the interested reader is referred to the Appendix in Porco and Nicholson (1987). Unless otherwise mentioned, all pattern speeds, resonant radii and predicted phases have been updated using satellite orbital elements from Jacobson et al. (2008b) and Saturn gravity field parameters from Jacobson et al. (2008a).

The resonances discussed here fall into one of two categories: Lindblad resonances, which produce radial forces and thus excite eccentricities in ring particle orbits; and vertical resonances, which produce normal forces and thus excite orbital inclinations. At a Lindblad resonance, the ring particle experiences radial force variations due to a particular component of the satellite's gravitational potential at a frequency equal to its natural radial oscillation, or epicyclic frequency κ. For a potential component that varies with longitude and time as $e^{i(m\lambda-\omega t)}$, the resonant condition is

$$m(n - \Omega_p) = \pm\kappa, \tag{20}$$

where n is the ring particle's keplerian angular velocity and the *pattern speed* of the potential is defined by its angular rotation rate $\Omega_p = \omega/m$. Noting that $\kappa = n - \dot{\varpi}_{\mathrm{sec}}$, we have the expression for Ω_p in Eq. (1) above. In Eq. (20) the + sign corresponds to an inner Lindblad resonance, where $n > \Omega_p$, and the − sign corresponds to an outer Lindblad resonance, where $n < \Omega_p$. We can in fact combine both ILRs and OLRs into a single expression for Ω_p by assigning a sign to m: positive for an ILR and negative for an OLR.

The situation is similar at a vertical resonance, where the ring particle experiences out-of-plane force variations at a frequency equal to its natural vertical oscillation frequency μ. For the same potential component, the resonant condition becomes

$$m(n - \Omega_p) = \pm\mu. \tag{21}$$

Noting that $\mu = n - \dot{\Omega}_{\rm sec}$, we have the expression for Ω_p given in Eq. (11) above. Again, both inner vertical resonances exist with $n > \Omega_p$ and outer vertical resonances with $n < \Omega_p$, which can be combined by assigning a sign to m.

A satellite on a circular, equatorial orbit gives rise to perturbations with all possible values of $|m|$, but all rotate at an angular frequency equal to the satellite's keplerian angular velocity, *i.e.*, $\Omega_p = n'$. Such perturbations lead to first-order Lindblad resonances, where

$$(m-1)n + \dot{\varpi}_{\rm sec} = mn'. \tag{22}$$

Examples of such resonances include the Prometheus 2:1 ILR at the outer edge of the Bond ringlet, with $m = 2$, and the Titan apsidal or 1:0 resonance, with $m = 1$.

A satellite on an eccentric and/or inclined orbit can give rise to a much richer spectrum of perturbations that also involve the satellite's own epicyclic and vertical frequencies κ' and μ'. In general, the frequency of such perturbations can be written as

$$\begin{aligned}\omega \equiv m\Omega_p &= mn' + k\kappa' + p\mu' \\ &= (m+k+p)n' - k\dot{\varpi}'_{\rm sec} - p\dot{\Omega}'_{\rm sec},\end{aligned} \tag{23}$$

where k and p are integers. Substituting this into Eq. (20) or Eq. (21), we have the condition to be satisfied at a higher-order Lindblad or vertical resonance:

$$(m-1)n + \dot{\varpi}_{\rm sec} = (m+k+p)n' - k\dot{\varpi}'_{\rm sec} - p\dot{\Omega}'_{\rm sec}, \tag{24}$$

or

$$(m-1)n + \dot{\Omega}_{\rm sec} = (m+k+p)n' - k\dot{\varpi}'_{\rm sec} - p\dot{\Omega}'_{\rm sec}. \tag{25}$$

Here, primed quantities refer to the perturbing satellite and unprimed quantities to the ring particle. Relevant examples of second-order resonances include the Mimas 3:1 ILR, with $m = 2,\ k = 1$ and $p = 0$, and the Mimas 3:1 IVR with $m = 2,\ k = 0$ and $p = 1$.

At each resonance, the response of ring particles is best described in terms of a slowly-changing resonance variable. For a Lindblad resonance this is given by

$$\phi_L = (m-1)\lambda + \varpi - (m+k+p)\lambda' + k\varpi' + p\Omega', \tag{26}$$

while for a vertical resonance it is

$$\phi_V = (m-1)\lambda + \Omega - (m+k+p)\lambda' + k\varpi' + p\Omega'. \tag{27}$$

Making use of the expression for Ω_p in Eq. (23), we can rewrite the satellite terms in these equations in the form $-m[\xi_0 + \Omega_p(t - t_0)]$, where the constant

$$\xi_0 = \left[(m+k+p)\lambda'_0 - k\varpi'_0 - p\Omega'_0\right]/m. \tag{28}$$

For particles located exactly at a Lindblad resonance, Eq. (24) implies that $d\phi_L/dt = 0$. An examination of the planetary perturbation equations shows that stable solutions exist only for $\phi = 0$ (generally for $a < a_{\rm res}$) or $\phi = \pi$ (for $a > a_{\rm res}$) (Murray and Dermott, 1999).

An ensemble of ring particles located at or near such a Lindblad resonance will move on eccentric orbits given approximately by the expression:

$$r(\lambda, t) \simeq a[1 - e\ \cos(\lambda - \varpi)]. \tag{29}$$

Substituting for ϖ in terms of ϕ_L and using Eqs. (23) and (28) above, this becomes

$$r(\lambda, t) \simeq a[1 - e\ \cos(m[\lambda - \xi_0 - \Omega_p(t - t_0)] - \phi_L)]. \tag{30}$$

This is the same as Eq. (5) in Section 4.1, where the phase angle $\delta_m = \xi_0 + \phi_L/m$.

At a vertical resonance Eq. (25) implies that $d\phi_V/dt = 0$. Starting with the analogous expression for particles moving on low-inclination orbits

$$z(\lambda, t) \simeq a\sin(i)\ \sin(\lambda - \Omega), \tag{31}$$

and substituting for Ω in terms of ϕ_V, we obtain

$$z(\lambda, t) \simeq a\sin(i)\ \sin(m[\lambda - \xi_0 - \Omega_p(t - t_0)] - \phi_V), \tag{32}$$

which is the same as Eq. (9) in Section 4.1, with the phase angle $\epsilon_m = \xi_0 + \phi_V/m$.

Using the above expressions for $\Omega_p,\ \delta_m$ and ϵ_m, we can calculate the relevant pattern speeds and predicted phases for each of the satellite resonances discussed above. For a first-order ILR, we have $k = p = 0$ so that $\Omega_p = n'$, as noted above, and $\xi_0 = \lambda'_0$, so that $\delta_m = \lambda'_0$ for orbits interior to $a_{\rm res}$, and $\delta_m = \lambda'_0 + \pi/m$ for orbits exterior to $a_{\rm res}$. For the Mimas 3:1 ILR, we have $m = 2,\ k = 1,\ p = 0$ so that $\Omega_p = (3n' - \dot{\varpi}'_{\rm sec})/2$ and $\delta_2 = (3\lambda'_0 - \varpi'_0 + \phi_L)/2$. For the Mimas 3:1 IVR, we have $m = 2,\ k = 0,\ p = 1$ so that $\Omega_p = \left(3n' - \dot{\Omega}'_{\rm sec}\right)/2$ and $\epsilon_2 = (3\lambda'_0 - \Omega'_0 + \phi_V)/2$. In Table 10 we list the corresponding numerical values for the five resonances discussed in Sections 5–8.

Also included in this table are estimates of the strength of each resonance $\mathcal{S}$, expressed in terms of the predicted amplitude of radial or vertical distortions at a distance of 1 km from the resonant radius $a_{\rm res}$. These strengths are taken from Nicholson and Porco (1988) and Table IV of Porco and Nicholson (1987), with the satellite masses and orbital elements updated to the values given by Jacobson et al. (2008b) or Spitale et al. (2006). For both Lindblad and vertical resonances in planetary rings, the forced amplitude, A_m or B_m is expected to vary as $\mathcal{S}/|a - a_{\rm res}|$, though this linear expression is likely to break down when the amplitude is comparable to $|a - a_{\rm res}|$, *i.e.*, for $|a - a_{\rm res}| < \sqrt{S}$. Closer to the resonance, streamline-crossing will occur in this simple model of noninteracting test-particles and, in reality, interparticle collisions and ring self-gravity will limit the maximum amplitude.

Table 10
Resonance parameters.[a]

Resonance	Titan 1:0 ILR	Mimas 3:1 IVR	Prom 2:1 ILR	Pand 2:1 ILR	Mimas 3:1 ILR
m	1	2	2	2	2
k	0	0	0	0	1
p	0	1	0	0	0
n' ($^\circ$ d^{-1})	22.5770	381.9835[b]	587.2852	572.7886	381.9835[b]
$\dot{\varpi}'$ ($^\circ$ d^{-1})	0.0014	1.0008	2.7577	2.5996	1.0008
$\dot{\Omega}'$ ($^\circ$ d^{-1})	−0.0014	−0.9995	−2.7444	−2.5874	−0.9995
Ω_p ($^\circ$ d^{-1})	22.5770	573.4750	587.2852	572.7886	572.4749
$a_{\rm res}$ (km)	77857.4	88702.2	88713.1	90167.8	90198.3
λ'_0 ($^\circ$)	97.5	347.2	22.9	25.8	347.2
ϖ'_0 ($^\circ$)	207.5	190.9	135	250	190.9
Ω'_0 ($^\circ$)	249.3	132.5	211	145	132.5
ξ_0 ($^\circ$)	97.5	94.6	22.9	25.8	65.4
δ_m or ϵ_m ($^\circ$)[c]	97.5	94.6	22.9	25.8	**65.4**
δ_m or ϵ_m ($^\circ$)[d]	**277.5**	184.6	**112.9**	**115.8**	155.4
$\mathcal{S}$ (km^2)	382	0.71	1.90	0.61	7.97

[a] At epoch 2008 January 1, 12:00 UTC = JD 2454467.0. See text for definitions.
[b] Average mean motion in 2005–2010.
[c] For ϕ_L or $\phi_V = 0^\circ$; expected values in bold face.
[d] For ϕ_L or $\phi_V = 180^\circ$; expected values in bold face.

References

Acton, C.H., 1996. Ancillary data services of NASA's navigation and ancillary information facility. Planet. Space Sci. 44, 65–70.

Baillié, K., Colwell, J.E., Lissauer, J.J., Esposito, L.W., Sremčević, M., 2011. Waves in Cassini UVIS stellar occultations. 2. The C ring. Icarus 216, 292–308.

Borderies, N., Goldreich, P., 1983. The variations in eccentricity and apse precession rate of a narrow ring perturbed by a close satellite. Icarus 53, 84–89.

Borderies, N., Longaretti, P.Y., 1987. Description and behavior of streamlines in planetary rings. Icarus 72, 593–603.

Borderies, N., Goldreich, P., Tremaine, S., 1983. The dynamics of elliptical rings. Astron. J. 88, 1560–1568.

Borderies, N., Goldreich, P., Tremaine, S., 1986. Nonlinear density waves in planetary rings. Icarus 68, 522–533.

Borderies, N., Gresh, D.L., Longaretti, P.Y., Marouf, E.A., 1988. Does self-gravity insure the Uranian ring rigid precession? Bull. Am. Astron. Soc. 20, 844.

Borderies-Rappaport, N., Longaretti, P.-Y., 1994. Test particle motion around an oblate planet. Icarus 107, 129–141.

Bosh, A.S., 1994. Stellar Occultation Studies of Saturn's Rings with the Hubble Space Telescope. Ph.D. Thesis, MIT, Cambridge.

Bosh, A.S., Olkin, C.B., French, R.G., Nicholson, P.D., 2002. Saturn's F ring: Kinematics and particle sizes from stellar occultation studies. Icarus 157, 57–75.

Brouwer, D., Clemence, G.M., 1961. Methods of Celestial Mechanics. Academic Press, New York.

Brown, R.H. et al., 2004. The Cassini visual and infrared mapping spectrometer (VIMS) investigation. Space Sci. Rev. 115, 111–168.

Chiang, E.I., Goldreich, P., 2000. Apse alignment of narrow eccentric planetary rings. Astrophys. J. 540, 1084–1090.

Colwell, J.E., Nicholson, P.D., Tiscareno, M.S., Murray, C.D., French, R.G., Marouf, E.A., 2009. The structure of Saturn's rings. In: Dougherty, M., Krimigis, S. (Eds.), Saturn After Cassini-Huygens. Springer, pp. 375–412.

Colwell, J.E., Esposito, L.W., Jerousek, R.G., Sremčević, M., Pettis, D., Bradley, E.T., 2010. Cassini UVIS stellar occultation observations of Saturn's rings. Astron. J. 140, 1569–1578.

ESA, 1997. The Hipparcos and Tycho catalogues. VizieR Online Data Catalog 1239, 0.

Esposito, L.W. et al., 1983. Eccentric ringlet in the Maxwell gap at 1.45 Saturn radii multi-instrument Voyager observations. Science 222, 57–60.

French, R.G., Elliot, J.L., Allen, D.A., 1982. Inclinations of the Uranian rings. Nature 298, 827–829.

French, R.G., Elliot, J.L., Levine, S.E., 1986. Structure of the Uranian rings. II – Ring orbits and widths. Icarus 67, 134–163.

French, R.G. et al., 1988a. Uranian ring orbits from Earth-based and Voyager occultation observations. Icarus 73, 349–378.

French, R.G., Longaretti, P., Smith, M., 1988b. Width-radius relations for Uranus' narrow rings. Bull. Am. Astron. Soc. 20, 845.

French, R.G., Nicholson, P.D., Porco, C.C., Marouf, E.A., 1991. Dynamics and structure of the Uranian rings. In: Bergstralh, J.T., Miner, E.D., Matthews, M.S. (Eds.), Uranus. University of Arizona Press, Tucson AZ, pp. 327–409.

French, R.G. et al., 1993. Geometry of the Saturn system from the 3 July 1989 occultation of 28 SGR and Voyager observations. Icarus 103, 163–214.

French, R.G., Marouf, E.A., Rappaport, N.J., McGhee, C.A., 2010a. Occultation observations of Saturn's B ring and Cassini division. Astron. J. 139, 1649–1667.

French, R.G., Nicholson, P.D., Colwell, J., Marouf, E.A., Rappaport, N.J., Hedman, M., Lonergan, K., McGhee-French, C., Sepersky, T. 2014a. Noncircular features in Saturn's Rings: III. The Cassini division. Icarus, in preparation.

French, R.G., et al., 2014b. Noncircular features in Saturn's rings: IV: Pole precession and radius scale, in preparation.

Goldreich, P., Tremaine, S., 1979. Precession of the epsilon ring of Uranus. Astron. J. 84, 1638–1641.

Hahn, J.M., Spitale, J.N., 2013. An N-body integrator for gravitating planetary rings, and the outer edge of Saturn's B ring. Bull. Am. Astron. Soc. 772, 122.

Hedman, M.M., Nicholson, P.D., 2013. Kronoseismology: Using density waves in Saturn's C ring to probe the planet's interior. Astron. J. 146, 12–27.

Hedman, M.M. et al., 2007. Saturn's dynamic D ring. Icarus 188, 89–107.

Hedman, M.M. et al., 2010. The architecture of the Cassini division. Astron. J. 139, 228–251.

Hedman, M.M., Burns, J.A., Evans, M.W., Tiscareno, M.S., Porco, C.C., 2011. Saturn's curiously corrugated C ring. Science 332, 708–711.

Hedman, M.M., Burt, J.A., Burns, J.A., Showalter, M.R., 2014. Non-circular features in Saturn's D ring: D68. Icarus 233, 147–162.

Jacobson, R.A. et al., 2006. The gravity field of the Saturnian system from satellite observations and spacecraft tracking data. Astron. J. 132, 2520–2526.

Jacobson, R.A., et al., 2008a. The Gravity Field of the Saturnian System and the Orbits of the Major Saturnian Satellites. Paper Presented at "Saturn after Cassini-Huygens Symposium, Imperial College, London.

Jacobson, R.A. et al., 2008b. Revised orbits of Saturn's small inner satellites. Astron. J. 135, 261–263.

Jacobson, R.A., et al., 2011. The Pole Orientation, Pole Precession, and Moment of Inertia Factor of Saturn. EPSC-DPS Joint Meeting 2011, 1070.

Jerousek, R.G., Colwell, J.E., Esposito, L.W., 2011. Morphology and variability of the Titan ringlet and Huygens ringlet edges. Icarus 216, 280–291.

Kliore, A.J. et al., 2004. Cassini radio science. Space Sci. Rev. 115, 1–70.

Longaretti, P.-Y., 1989. Uranian ring dynamics – An analysis of multimode motions. Icarus 82, 281–287.

Longaretti, P.-Y., Rappaport, N., 1995. Viscous overstabilities in dense narrow planetary rings. Icarus 116, 376–396.

Marouf, E.A., Gresh, D.L., Tyler, G.L., 1987. Eccentricity gradients of Uranus' epsilon, beta, and alpha rings. Bull. Am. Astron. Soc. 19, 883.

Melita, M.D., Papaloizou, J.C.B., 2005. Resonantly forced eccentric ringlets: Relationships between surface density, resonance location, eccentricity and eccentricity-gradient. Cel. Mech. Dyn. Astron. 91, 151–171.

Mosqueira, I., 1996. Local simulations of perturbed dense planetary rings. Icarus 122, 128–152.

Mosqueira, I., Estrada, P.R., 2002. Apse alignment of the Uranian rings. Icarus 158, 545–556.

Murray, C.D., Dermott, S.F., 1999. Solar System Dynamics. Cambridge University Press.

Nicholson, P.D., Matthews, K., 1983. Surface densities and velocity dispersions of the Uranian rings. Bull. Am. Astron. Soc. 15, 816.

Nicholson, P.D., Porco, C.C., 1988. A new constraint on Saturn's zonal gravity harmonics from Voyager observations of an eccentric ringlet. J. Geophys. Res. 93, 10209–10224.

Nicholson, P.D., Cooke, M.L., Pelton, E., 1990. An absolute radius scale for Saturn's rings. Astron. J. 100, 1339–1362.

Nicholson, P.D., French, R.G., Hedman, M.M., Marouf, E.A., Colwell, J.E., 2014. Noncircular features in Saturn's rings: I. The edge of the B ring. Icarus 227, 152–175.

Null, G.W., Lau, E.L., Biller, E.D., Anderson, J.D., 1981. Saturn gravity results obtained from Pioneer 11 tracking data and Earth-based Saturn satellite data. Astron. J. 86, 456–468.

Porco, C.C., Nicholson, P.D., 1987. Eccentric features in Saturn's outer C ring. Icarus 72, 437–467.

Porco, C., Nicholson, P.D., Borderies, N., Danielson, G.E., Goldreich, P., Holberg, J.B., Lane, A.L., 1984b. The eccentric Saturnian ringlets at 1.29 R_S and 1.45 R_S. Icarus 60, 1–16.

Porco, C.C. et al., 2005. Cassini imaging science: Initial results on Saturn's rings and small satellites. Science 307, 1226–1236.

Shu, F.H., 1984. Waves in planetary rings. In: Brahic, A., Greenberg, R. (Eds.), IAU Colloq. 75: Planetary Rings. Univ. of Arizona Press, pp. 513–561.

Spitale, J.N., Jacobson, R.A., Porco, C.C., Owen Jr., W.M., 2006. The orbits of Saturn's small satellites derived from combined historic and Cassini imaging observations. Astron. J. 132, 692–710.

Spitale, J.N., Porco, C.C., 2010. Detection of free unstable modes and massive bodies in Saturn's outer B ring. Astron. J. 140, 1747–1757.